



This is to certify that the

thesis entitled

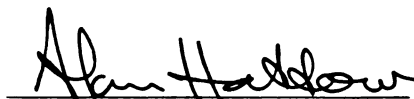
CHAOTIC AND PERIODIC DYNAMICS OF A  
SLIDER CRANK MECHANISM WITH SLIDER  
CLEARANCE

presented by

FARAMARZ FARAHANCHI

has been accepted towards fulfillment  
of the requirements for

M.S. degree in MECHANICAL ENGINEERING



Major professor

Date 11-11-1991

**CHAOTIC AND PERIODIC DYNAMICS OF A  
SLIDER CRANK MECHANISM WITH  
SLIDER CLEARANCE**

**By**

**Faramarz Farahanchi**

**A THESIS**

**Submitted to  
Michigan State University  
in partial fulfillment of the requirements  
for the degree of**

**MASTER OF SCIENCE**

**Department of Mechanical Engineering**

**1991**

## **ABSTRACT**

# **CHAOTIC AND PERIODIC DYNAMICS OF A SLIDER CRANK MECHANISM WITH SLIDER CLEARANCE**

**BY**

**Faramarz Farahanchi**

Bearing clearance is one of the most important factors influencing the dynamic performance and durability of mechanisms. In this thesis, the problem of a planar slider crank mechanism with clearance at the sliding bearing is investigated. This problem is relevant to the phenomenon known as piston slap to automotive engineers. In this study the influence of the clearance gap size, bearing friction, crank speed, and impact parameters on the response of the system are investigated. Three types of response are observed: chaotic, transient chaos, and periodic. It is shown that chaotic motion is prevalent over a range of parameters which corresponds to high crank speeds and/or low values of the bearing friction with relatively ideal impacts. Periodic response is generally observed at low crank speeds and also at low values of the coefficient of restitution. Poincare maps and statistical profiles of the impact locations and severity are used to characterize the motion and to obtain information regarding possible patterns of wear due to repeated impacts. As expected, chaotic motions lead to quite uniform distributions of impacts while periodic motions lead to highly localized impact locations. Hence, chaotic motions may be beneficial, as they provide a more desirable pattern of impacts.

**TO MY PARENTS**

## ACKNOWLEDGEMENTS

I would like to this opportunity to express my sincere gratitude to the following people. First of all, I would like to thank my thesis advisor Dr. Steven W. Shaw. His endless patience, guidance, help, and suggestions during my research and graduate work is greatly appreciated. It has been a great privilege to work with him.

My especial thanks goes to Dr. Alan G. Haddow for being in my graduate committee and agreeing to be my supervising advisor. I would also like to thank Dr. Alejandro Diaz and Dr. Philip Fitzsimons for agreeing to serve as my committee members.

I would also like to thank National Science Foundations for their support of this investigation.

Finally, I would like to thank my parents and my grandparents for their support and encouragements.

# Contents

<b>List of Figures</b>	<b>vii</b>
<b>1 Introduction</b>	<b>1</b>
<b>2 Mathematical Model</b>	<b>4</b>
2.1 Basic Assumptions . . . . .	4
2.2 Derivation of the Equation of Motion for Free Flight Motion . . . . .	6
2.3 Nondimensionalization . . . . .	10
2.4 Linearization in $\psi$ . . . . .	12
2.5 Impact Conditions . . . . .	13
2.6 Sliding Conditions . . . . .	16
<b>3 Methods of Analysis</b>	<b>29</b>
3.1 Poincare Section . . . . .	29
3.2 Impact Distribution Profile . . . . .	32
3.3 Impact Spectra . . . . .	34
<b>4 Results</b>	<b>35</b>

4.1	Introduction . . . . .	35
4.2	General Observation of Chaotic Motion . . . . .	37
4.3	Non-sliding Dynamics . . . . .	41
4.4	Dynamics Involving Sliding . . . . .	49
<b>5</b>	<b>Discussions and Future Direction for Research</b>	<b>60</b>
<b>A</b>	<b>Derivation of <math>\psi_{maz}</math> and <math>\psi_{min}</math></b>	<b>64</b>
<b>B</b>	<b>Simulation Routine</b>	<b>68</b>
	<b>Bibliography</b>	<b>71</b>



# List of Figures

2.1	Schematic view of the model . . . . .	6
2.2	The Constraints for $\psi$ . . . . .	15
2.3	The model through the virtual displacement of the roller . . . . .	19
2.4	Constraint force on the roller at $\lambda = 0.01$ . . . . .	23
2.5	Constraint force on the roller at $\lambda = 0.1$ . . . . .	24
2.6	Constraint force on the roller at $\lambda = 0.25$ . . . . .	25
2.7	Constraint force on the roller at $\lambda = 0.267$ , $\rho = 0.02$ . . . . .	25
2.8	Blow up of the constraint force on the roller . . . . .	26
2.9	Constraint force on the roller at $\lambda = 0.35$ . . . . .	27
2.10	Regions of Sliding on the Supporting Structure. . . . .	28
3.1	Three Dimensional phase space, with the restriction . . . . .	31
4.1	Time Trace . . . . .	38
4.2	Phase Portrait . . . . .	38
4.3	Poincare Map, $\lambda = 0.05$ and $\rho = 0.01$ . . . . .	39
4.4	First Magnification of Poincare Map . . . . .	40
4.5	Second Magnification of Poincare Map . . . . .	40

4.6	Impact Distribution Pattern, $\lambda = 0.025$ and $\rho = 0.010$ . . . . .	42
4.7	Impact Distribution Pattern, $\lambda = 0.025$ and $\rho = 0.015$ . . . . .	42
4.8	Impact Distribution Pattern, $\lambda = 0.025$ and $\rho = 0.020$ . . . . .	42
4.9	Impact Distribution Pattern, $\lambda = 0.05$ and $\rho = 0.010$ . . . . .	43
4.10	Impact Distribution Pattern, $\lambda = 0.05$ and $\rho = 0.015$ . . . . .	43
4.11	Impact Distribution Pattern, $\lambda = 0.05$ and $\rho = 0.020$ . . . . .	43
4.12	Impact Distribution Pattern, $\lambda = 0.075$ and $\rho = 0.010$ . . . . .	44
4.13	Impact Distribution Pattern, $\lambda = 0.075$ and $\rho = 0.015$ . . . . .	44
4.14	Impact Distribution Pattern, $\lambda = 0.075$ and $\rho = 0.020$ . . . . .	44
4.15	Poincare Map, $\lambda = 0.05$ and $\rho = 0.015$ . . . . .	45
4.16	Impact Spectra, Upper Wall $\lambda = 0.05$ and $\rho = 0.015$ . . . . .	45
4.17	Impact Spectra, Lower Wall $\lambda = 0.05$ and $\rho = 0.015$ . . . . .	45
4.18	Poincare Map, $\lambda = 0.025$ and $\rho = 0.01$ . . . . .	46
4.19	Impact Spectra, Upper Wall $\lambda = 0.025$ and $\rho = 0.01$ . . . . .	46
4.20	Impact Spectra, Lower Wall $\lambda = 0.025$ and $\rho = 0.01$ . . . . .	46
4.21	Poincare Map, $\lambda = 0.075$ and $\rho = 0.02$ . . . . .	47
4.22	Impact Spectra, Upper Wall $\lambda = 0.075$ and $\rho = 0.02$ . . . . .	47
4.23	Impact Spectra, Lower Wall $\lambda = 0.075$ and $\rho = 0.02$ . . . . .	47
4.24	Impact Distribution Pattern, $\lambda = 0.15$ and $\rho = 0.010$ . . . . .	50
4.25	Impact Distribution Pattern, $\lambda = 0.15$ and $\rho = 0.015$ . . . . .	50
4.26	Impact Distribution Pattern, $\lambda = 0.15$ and $\rho = 0.020$ . . . . .	50
4.27	Impact Distribution Pattern, $\lambda = 0.20$ and $\rho = 0.010$ . . . . .	51
4.28	Impact Distribution Pattern, $\lambda = 0.20$ and $\rho = 0.015$ . . . . .	51

4.29 Impact Distribution Pattern, $\lambda = 0.20$ and $\rho = 0.020$ . . . . .	51
4.30 Impact Distribution Pattern, $\lambda = 0.25$ and $\rho = 0.010$ . . . . .	52
4.31 Impact Distribution Pattern, $\lambda = 0.25$ and $\rho = 0.015$ . . . . .	52
4.32 Impact Distribution Pattern, $\lambda = 0.25$ and $\rho = 0.020$ . . . . .	52
4.33 Poincare Map, $\lambda = 0.2$ and $\rho = 0.015$ . . . . .	53
4.34 Poincare Map, $\lambda = 0.25$ and $\rho = 0.015$ . . . . .	53
4.35 Time Trace, $e = 0.9, \lambda = 0.25$ , and $\rho = 0.015$ . . . . .	54
4.36 Poincare Map, $\lambda = 0.25$ and $\rho = 0.01$ . . . . .	54
4.37 Poincare Map, $\lambda = 0.25$ and $\rho = 0.02$ . . . . .	55
4.38 Poincare Map, $e = 0.7, \lambda = 0.05$ , and $\rho = 0.02$ . . . . .	56
4.39 Poincare Map, $e = 0.5, \lambda = 0.05$ , and $\rho = 0.02$ . . . . .	56
4.40 Impact Dist. Pattern, $e = 0.7, \lambda = 0.025$ , and $\rho = 0.020$ . . . . .	57
4.41 Impact Dist. Pattern, $e = 0.5, \lambda = 0.025$ , and $\rho = 0.020$ . . . . .	57
4.42 Time Trace, $e = 0.9, \lambda = 0.05$ , and $\rho = 0.02$ . . . . .	58
4.43 Time Trace, $e = 0.7, \lambda = 0.05$ , and $\rho = 0.02$ . . . . .	59
4.44 Time Trace, $e = 0.5, \lambda = 0.05$ , and $\rho = 0.02$ . . . . .	59
A.1 The maximum angle . . . . .	64
B.1 Flow Chart: Simulation Routine . . . . .	70

# Chapter 1

## Introduction

Of the many factors which influence the dynamic performance and durability of mechanisms, one of the most important is bearing clearance. Such clearances often lead to high localized stresses and thus to increased fatigue, noise, and wear. In this thesis we choose a simple model problem which is of interest in automotive applications in order to show that the dynamic response of such systems, which has been known to be quite complicated, can, in fact, be chaotic. We also describe the influence of various system parameters on the response and provide means of displaying data which may be helpful in understanding patterns of fretting and wear.

The problem under investigation is a slider crank mechanism with clearance between the slider and its supporting structure. This problem is relevant to the phenomenon known as piston slap to automotive engineers. Due to the clearance, repeated impacts occur between the slider and its supporting structure, resulting in fatigue, dynamical stress, noise, and wear. In order to control these effects, one must understand the underlying dynamics.

In recent years, the effects of clearance at the joints of mechanical systems has been studied by many researchers. Most closely related to the present work is that of Wilson and Fawcett [11] who considered the case of a slider crank mechanism with clearance at the sliding bearing. They consider all possible impact configurations of the slider using a two degree of freedom model and present simulation results for that model. Other researchers have considered clearance at revolute joints in mechanisms using a variety of methods. The research done in this area includes studies of the response of rigid link systems with clearances at joints [15, 16, 6, 17], as well as those with joint clearance and flexible links [18, 19]. Some investigations have considered systems in which only a single joint has clearance [15, 16, 6, 17], while others consider clearances in several of the joints of the mechanism [20, 21].

In these investigations, several different approaches are proposed. Grant and Fawcett [7] suggested methods for predicting contact loss and a method of preventing loss of contact. Dubowsky and Norris [8] provide an analytical and experimental study for prediction of impact and they defined the Impact Prediction Number (IPN) which correctly predicts the trends observed in their study. Dubowsky and Gardener [18] considered multi-link flexible mechanisms with multiple clearance connections. The methodology employed in that study was a perturbation coordinate approach and it was shown that simpler models yield useful insights into behavior of the more complex systems. Mansour and Townsend [9] took a momentum-exchange approach in their study of impacts at a joint. They studied the local and path-spectra of the impacts between the socket and the connecting pin and from these the dominant impacts at the joints were identified and investigated.

In the work presented here, the problem of the planar slider crank mechanism with clearance between a cylindrical slider and its supporting structure is investigated. The equations of motion for the system are derived by using Lagrange's method along with a simple impact rule, and these are investigated by numerical solutions and Poincare maps. The response of the system appears to be generally chaotic over a wide range of parameters although periodic motions become more common as dissipation effects are increased. Having determined the response of the system, techniques developed in recent years, such as Poincare maps, are applied for further investigation of the response.

Other studies along similar lines include that of Karagiannis [13] who studied the problem of gear backlash. He has developed an understanding of the periodic and chaotic behavior of gear backlash by applying similar methods. Pfeiffer and Kunert [14] have also applied these methods to the problem of rattling in gears due to backlash. In addition, Shaw [1] has studied the response of an oscillator with constraints subjected to harmonic excitation by using similar methods.

This thesis is arranged as follows. The underlying assumptions and the equations of motion for the system under study are provided in Chapter 2. Chapter 3 describes the methods of analysis. Chapter 4 contains the main results and describes the influence of various important system parameters on features of the response by using simulations. A discussion and directions for future research are provided in Chapter 5. Some detailed derivations and a summary of the simulation routine are provided in the appendices.

# Chapter 2

## Mathematical Model

In this chapter we describe the model employed and derive the equations which govern its dynamics. The basic assumptions are provided first. Next, the differential equation which describes the free flight dynamics, that is, the motion between impacts, is derived. It is nondimensionalized and then linearized based on a small clearance assumption. The rules which govern the impact dynamics are then presented. Also, a complete discussion regarding the possible regions of potential sliding and the attendant constraint forces is included. This provides a complete set of dynamic equations which are studied in subsequent chapters.

### 2.1 Basic Assumptions

In order to provide some insight into the effects of clearances on the motion of a connecting rod / piston assembly in a slider crank mechanism, we introduce a simplified model, shown in Figure 2.1, which employs the following assumptions:

- All motions occur in a fixed plane.
- All components are rigid.
- The bearings joining the connecting rod to the crank and the piston have no clearance.
- The bearing which connects the connecting rod to the crank provides a viscous type frictional moment which is proportional to the relative rotational rate between the crank and connecting rod.
- The crank speed is constant.
- The nominal mechanism, that is, the one without clearance, is an on-line slider crank.
- The clearances for the piston are symmetrically placed about the nominal piston path and have a fixed magnitude along the cylinder wall.
- Gravitational effects are ignored. This is valid when the mechanism lies in a horizontal plane or when the crank speed is sufficiently large that inertial forces dominate the response.
- The piston is a cylindrical roller which is attached to the connecting rod at its geometric center. This simple geometry allows for the isolation of the effects of the clearance from complications associated with the piston geometry. It also reduces the mechanism to a single degree of freedom system, since the piston orientation does not affect the dynamics.



- Impacts between the piston and the walls are instantaneous and modeled by a simple impact rule which employs a constant coefficient of restitution.

## 2.2 Derivation of the Equation of Motion for Free Flight Motion

For deriving the equation of motion, the Lagrangian approach is used. To apply the Lagrangian method, the kinetic energy and potential energy of each component is required. Based on the assumptions made in the previous section, there is no potential energy in any component of the system. In order to obtain the kinetic energy of each component, the center of mass velocity and angular velocity of each component is required.

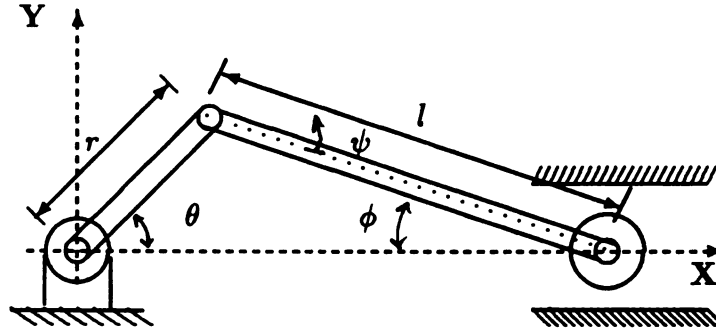


Figure 2.1: Schematic view of the model

For the generalized coordinate which describes the configuration of the system we choose  $\psi$ , the angle which measures the deviation of the connecting rod centerline from its nominal (that is, zero clearance) orientation; see Figure 2.1. This angle is chosen since it will remain small when the clearance is small.

From Figure 2.1 the displacement of the center of mass of the uniform connecting rod can be expressed in terms of  $\psi$ , the angle measuring the deviation of the connecting rod from its nominal position,  $\phi$ , the angle between the nominal position of the connecting rod and the horizontal, and  $\theta$ , the crank angle measured as indicated in Figure 2.1, as follows:

$$\begin{aligned}x_r &= r \cos \theta + \frac{1}{2} l \cos (\phi - \psi) \\y_r &= r \sin \theta - \frac{1}{2} l \sin (\phi - \psi)\end{aligned}$$

Note that  $\phi$  and  $\theta$  are related; this will be subsequently exploited.

By taking the time derivative of the above displacements, the horizontal and vertical velocities of the connecting rod center of mass can be expressed in terms of  $\phi$ ,  $\psi$ , and  $\theta$  as follows

$$\begin{aligned}\dot{x}_r &= -r \dot{\theta} \sin \theta - \frac{1}{2} l (\dot{\phi} - \dot{\psi}) \sin (\phi - \psi) \\ \dot{y}_r &= r \dot{\theta} \cos \theta - \frac{1}{2} l (\dot{\phi} - \dot{\psi}) \cos (\phi - \psi)\end{aligned}$$

By using the above velocities and the angular velocity of the connecting rod,  $\dot{\phi} + \dot{\psi}$ , the kinetic energy of the connecting rod is obtained

$$T_r = \frac{1}{2} m (\dot{x}_r^2 + \dot{y}_r^2) + \frac{1}{2} J_r (\dot{\phi} + \dot{\psi})^2 \quad (2.1)$$



or

$$T_r = \frac{1}{2} m \left\{ \left[ -r \dot{\theta} \sin \theta - \frac{1}{2} l (\dot{\phi} - \dot{\psi}) \sin (\phi - \psi) \right]^2 + \left[ r \dot{\theta} \cos \theta - \frac{1}{2} l (\dot{\phi} - \dot{\psi}) \cos (\phi - \psi) \right]^2 \right\} + \frac{1}{2} J_r (\dot{\phi} + \dot{\psi})^2 \quad (2.2)$$

where  $m$  is the mass of the connecting rod and  $J_r$  is the moment of inertia of the connecting rod about its mass center.

From Figure 2.1 the displacement of the center of slider in terms of  $\phi$ ,  $\psi$ , and  $\theta$  is determined to be

$$x_s = r \cos \theta + l \cos (\phi - \psi)$$

$$y_s = r \sin \theta - l \sin (\phi - \psi)$$

By taking time derivatives of these, the horizontal and vertical velocities of the slider are obtained

$$\dot{x}_s = -r \dot{\theta} \sin \theta - l (\dot{\phi} - \dot{\psi}) \sin (\phi - \psi)$$

$$\dot{y}_s = r \dot{\theta} \cos \theta - l (\dot{\phi} - \dot{\psi}) \cos (\phi - \psi)$$

Note that in the absence of clearance the vertical position and velocity of the slider piston must be zero. This can be verified by using the geometry of the nominal mechanism. Due to the rotational symmetry of the slider mass, its angular orientation is inconsequential to the response of the system and thus only its translation is of

interest here. The relevant kinetic energy of the slider is

$$T_s = \frac{1}{2} M (\dot{x}_s^2 + \dot{y}_s^2) \quad (2.3)$$

or

$$\begin{aligned} T_s = & \frac{1}{2} M \{ [-r\dot{\theta} \sin \theta - l(\dot{\phi} - \dot{\psi}) \sin(\phi - \psi)]^2 \\ & + [r\dot{\theta} \cos \theta - l(\dot{\phi} - \dot{\psi}) \cos(\phi - \psi)]^2 \} \end{aligned} \quad (2.4)$$

where  $M$  is the mass of the slider piston.

Having obtained expressions for the kinetic energies of the components, the total kinetic energy of the system is then expressed as

$$\begin{aligned} T_{total} &= T_r + T_s \\ T_{total} &= \frac{1}{2} m (\dot{x}_r^2 + \dot{y}_r^2) + \frac{1}{2} J_r (\dot{\phi} + \dot{\psi})^2 + \frac{1}{2} M (\dot{x}_s^2 + \dot{y}_s^2) \\ T_{total} &= \frac{1}{2} m \{ [-r\dot{\theta} \sin \theta - \frac{1}{2} l(\dot{\phi} - \dot{\psi}) \sin(\phi - \psi)]^2 \\ &+ [r\dot{\theta} \cos \theta - \frac{1}{2} l(\dot{\phi} - \dot{\psi}) \cos(\phi - \psi)]^2 \} + \frac{1}{2} J_r (\dot{\phi} + \dot{\psi})^2 \\ &+ \frac{1}{2} M \{ [-r\dot{\theta} \sin \theta - l(\dot{\phi} - \dot{\psi}) \sin(\phi - \psi)]^2 \\ &+ [r\dot{\theta} \cos \theta - l(\dot{\phi} - \dot{\psi}) \cos(\phi - \psi)]^2 \} \end{aligned} \quad (2.5)$$

The frictional moment at the crank-connecting rod connection is assumed to be proportional to the relative angular velocity of the components connected there. The

resulting dissipative moment on the connecting rod can be expressed as

$$M_2 = -c_2(-\dot{\theta} - \dot{\phi} + \dot{\psi}) \quad (2.6)$$

For determining the equation of motion, Lagrange's method is then applied:

$$\frac{d}{dt}\left(\frac{\partial L}{\partial \dot{q}}\right) - \frac{\partial L}{\partial q} = Q' \quad (2.7)$$

where

$$q = \psi$$

$$Q' = -c_2(-\dot{\theta} - \dot{\phi} + \dot{\psi})$$

$$L = T_{total}$$

which results in the following equation of the motion for the system

$$\begin{aligned} & \frac{1}{2} m \{ -\Omega^2 r l [\sin \Omega t \cos(\phi - \psi) - \cos \Omega t \sin(\phi - \psi)] - \frac{1}{2} l^2 (\ddot{\phi} - \ddot{\psi}) \} \\ & - M \{ \Omega^2 r l [\sin \Omega t \cos(\phi - \psi) + \cos \Omega t \sin(\phi - \psi) + l^2 (\ddot{\phi} - \ddot{\psi})] \} \\ & + J_r (\ddot{\phi} + \ddot{\psi}) = -c_2 (-\dot{\theta} - \dot{\phi} + \dot{\psi}) \end{aligned} \quad (2.8)$$

## 2.3 Nondimensionalization

It is convenient to present the equation of motion in dimensionless form. By nondimensionalizing, the number of parameters associated with the equation of motion is

reduced. In order to nondimensionalize the equation of motion, both sides of the equation are first divided by  $MI^2\Omega^2$  as follows:

$$\begin{aligned} & \frac{m}{2MI^2\Omega^2} \{ -\Omega^2 r l [\sin \Omega t \cos(\phi - \psi) + \cos \Omega t \sin(\phi - \psi)] - \frac{1}{2} l^2 (\ddot{\phi} - \ddot{\psi}) \} \\ & - \frac{M}{MI^2\Omega^2} \{ \Omega^2 r l [\sin \Omega t \cos(\phi - \psi) + \cos \Omega t \sin(\phi - \psi) + l^2 (\ddot{\phi} - \ddot{\psi})] \} \\ & + \frac{J_r}{MI^2\Omega^2} (\ddot{\phi} + \ddot{\psi}) = \frac{-c_2}{MI^2\Omega^2} (-\dot{\theta} - \dot{\phi} + \dot{\psi}) \end{aligned} \quad (2.9)$$

Then, by defining the following dimensionless parameters and variables

$$\begin{aligned} \xi &= \frac{r}{l} \\ \alpha &= \frac{m}{M} \\ \beta &= \frac{J_r}{MI^2} \\ \lambda &= \frac{c_2}{MI^2\Omega} \\ \Lambda &= \sqrt{1 - \xi^2 \sin^2 \tau} \\ \tau &= \Omega t \\ ( )' &= \Omega ( \dot{ } ) \end{aligned}$$

the dimensionless equation of motion is obtained by straightforward rescaling. It is given by

$$\begin{aligned}
& -\frac{1}{2} \alpha \{ \xi [ \sin \tau \cos (\phi - \psi) + \cos \tau \sin (\phi - \psi) ] + \frac{1}{2} ( \phi'' - \psi'' ) \} \\
& - \{ \xi [ \sin \tau \cos (\phi - \psi) + \cos \tau \sin (\phi - \psi) ] + ( \phi'' - \psi'' ) \} \\
& + \beta ( \phi'' + \psi'' ) = -\lambda ( -1 - \phi' + \psi' )
\end{aligned} \tag{2.10}$$

## 2.4 Linearization in $\psi$

Note that, from Figure 2.1,  $\phi$  can be written in terms of  $\theta$  based on the following constraint equation

$$l \sin \phi = r \sin \theta \tag{2.11}$$

or in dimensionless form

$$\sin \phi = \xi \sin \tau \tag{2.12}$$

since  $\tau = \Omega t = \theta$ .

Since  $\psi$  will be restricted to small angles for all reasonable clearances, the following approximations can be used for  $\psi$

$$\cos \psi = 1 + \mathcal{O}(\psi^2)$$

$$\sin \psi = \psi + \mathcal{O}(\psi^3)$$

By using the above assumptions, retaining only those terms linear in  $\psi$  and derivatives of  $\psi$ , and utilizing equation 2.12, the equation of motion can be expressed



in linearized form in terms of  $\psi$ . The dimensionless, linearized equation of motion is given by

$$a \psi'' + b \psi' + c(\tau)\psi = f(\tau) \quad (2.13)$$

where

$$\begin{aligned} a &= \frac{1}{4}\alpha + 1 + \beta \\ b &= \lambda \\ c(\tau) &= (1 + \frac{1}{2}\alpha) \xi \Lambda \cos \tau - (1 + \frac{1}{2}\alpha) \xi^2 \sin^2 \tau \\ f(\tau) &= (\frac{1}{4}\alpha + 1 - \beta) \frac{(\xi^3 - \xi) \sin \tau}{\Lambda^3} + (\xi \Lambda + \frac{1}{2}\alpha \xi \Lambda) \sin \tau \\ &\quad + (\frac{1}{2}\xi^2 + \frac{1}{4}\xi^2 \alpha) \sin 2\tau + \lambda + \frac{\lambda \xi \cos \tau}{\Lambda} \end{aligned}$$

Note that in the equation of motion (i.e., equation 2.13), the only dimensionless system parameter that depends on the crank frequency  $\Omega$  is the dissipation parameter,  $\lambda$ . This implies that a study which varies  $\lambda$  is equivalent to one which varies the crank operating speed. Also note that the equation of motion has both external and parametric excitation which arise from the gross motion of the connecting rod. The solution of this equation of motion describes the motion of the connecting rod during flights between the barriers.

## 2.5 Impact Conditions

The magnitude of the clearance is described by the difference between the slider radius (in the plane of motion),  $r^*$ , and the distance from the nominal piston motion

centerline to the cylinder wall,  $d$ . Thus the piston is free to move a distance  $d - r^*$  up or down from its nominal position.

Based on this gap the motion of the connecting rod is restricted to lie in a region  $\psi_{min} \leq \psi \leq \psi_{max}$ . From the geometry of the model, for  $|\psi| \ll 1$  the maximum and minimum values that  $\psi$  can achieve can be shown to be given by

$$\psi_{max} = \frac{\rho}{\sqrt{1 - \xi^2 \sin^2 \tau}} \quad (2.14)$$

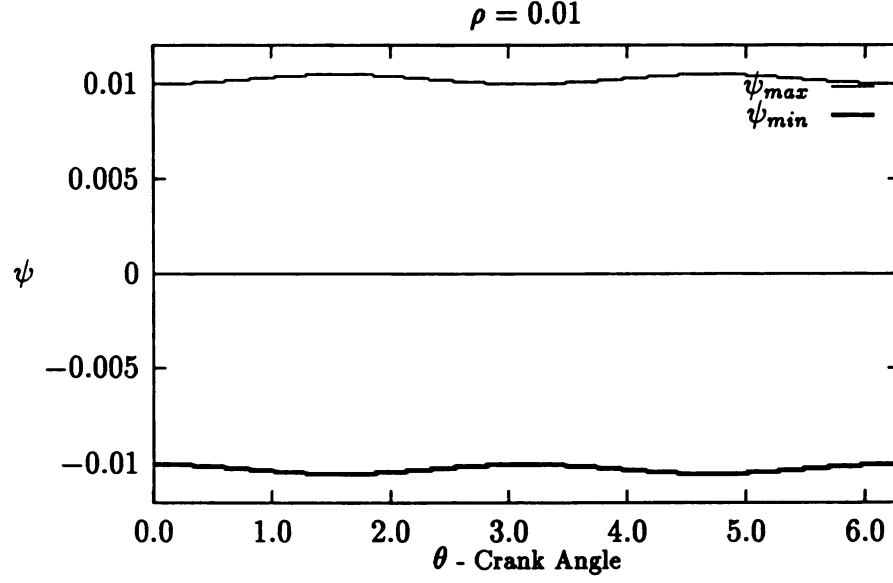
$$\psi_{min} = \frac{-\rho}{\sqrt{1 - \xi^2 \sin^2 \tau}} \quad (2.15)$$

where

$$\rho = \frac{d - r^*}{l}$$

is the dimensionless gap size. Note that  $\psi_{max} = -\psi_{min}$  is valid only for linearized case (i.e. under the assumption of small gap size). A detailed derivation of  $\psi_{max}$  and  $\psi_{min}$  are provided in Appendix A.

Figure 2.2 depicts the time dependent region in which  $\psi$  can lie without impact occurring. Note that impact occurs whenever  $\psi = \psi_{max}$  or  $\psi = \psi_{min}$  is satisfied during a given motion. A simple impact rule is assumed in which the relative velocity after impact is proportional to the relative velocity before impact, with the constant of proportionality equal to the negative of the coefficient of restitution [24]. This is done by using the vertical component of the absolute velocity of the slider center,  $\dot{y}_s$ . This is the natural velocity to use since it is normal to the impact surface and

Figure 2.2: The Constraints for  $\psi$ 

since it gives the relative velocity between the slider and the stationary supporting structure. The impact rule is given by

$$\dot{y}_{s_{after}} = -e \dot{y}_{s_{before}} \quad (2.16)$$

Using the expression for  $\dot{y}_s$  from section 2.2, nondimensionalizing, linearizing in  $\psi$ , and solving for  $\dot{\psi}_{after}$  leads to the following expression for the velocity after impact in terms of  $\dot{\psi}$ :

$$\dot{\psi}_{after} = (1 + e) \left[ \frac{\xi^2 \sin \tau \cos \tau}{\Lambda^2} \psi \right] - e \dot{\psi}_{before} \quad (2.17)$$

where

$$e \equiv \text{Coefficient of restitution}$$

and  $\psi = \psi_{max}$  or  $\psi = \psi_{min}$ .

Note that  $\dot{\psi}_{after}$  is found by assuming simple impacts between the roller and the wall of the cylinder. In simulations the exact location and time of the impact is determined in the simulations by applying Newton's root solving method to the conditions  $\psi = \psi_{max}$  or  $\psi = \psi_{min}$  (see Appendix B for details).

We now have a complete set of dynamic equations. Equation 2.13 gives the free flight and equations 2.14, 2.15, and 2.17 determine the impact conditions. It should be noted that since an infinite number of impacts can occur in finite time, sliding motions may occur in which  $\psi = \psi_{max}$  or  $\psi = \psi_{min}$  for finite time durations (see Wilson and Fawcett [11]); this is considered in the following section.

## 2.6 Sliding Conditions

In the problem under investigation there are occasions in which the roller may slide along the supporting structure. This occurs when several impacts occur close together in such a manner that the relative velocity goes to zero via an infinite number of impacts which occur in finite time. This is analogous to the simple problem of dropping an inelastic ball on a rigid surface and letting it bounce; it similarly comes to rest in a finite time after an infinite number of impacts ( Greenwood [25], pp 160-161 ). In the mechanism under consideration, this typically occurs when the friction at the joint connecting the crank and the connecting rod is large, or if the coefficient of restitution is small, or some combination of these conditions.

The analysis of sliding motions is carried out as follows. We begin by computing

the normal forces between the roller and the supporting structure under the assumption that the roller moves along paths  $\psi = \psi_{max}$  or  $\psi = \psi_{min}$ . These are the forces which would be required to maintain contact and will represent the actual contact forces in these cases in which the force is compressive. A tensile force is non-physical and occurs in regions where sliding will not occur. For a given set of parameters  $(\lambda, \rho)$  as the crank advances these forces vary and change direction at certain crank angles. At those angles where the force changes from compression to tension, the roller, if sliding, will be released into free motion between the constraints. Crank angles at which the force changes from tension to compression correspond to the beginning of crank angle intervals in which sliding can occur on the corresponding constraint. This analysis indicates that there exists four types of crank angle regions:

- those in which sliding can occur only along the upper constraint,
- those in which sliding can occur only along the lower constraint,
- those where sliding can not occur along either constraint.
- those where sliding can occur along either constraint.

Depending on  $\rho$  and  $\lambda$ , the crank angle may be broken into distinct intervals of these types. It should be remembered that free flight can occur in any region, and that sliding will occur in the allowed region only under certain conditions.

The constraint force is derived using the principle of virtual work and Lagrange's method. The procedure is to first obtain the equation of motion for an unconstrained connecting rod with and applied vertical force on the roller. The constraints

$\psi = \psi_{max}$  and  $\psi = \psi_{min}$  are then substituted into the equation of motion and the resulting applied forces , i.e. those required to maintain contact on the lower and upper constraints, respectively, are solved for directly.

Lagrange's equation for this case is given by

$$\frac{d}{dt}\left(\frac{\partial T}{\partial \dot{\psi}}\right) - \frac{\partial T}{\partial \psi} = Q + Q' \quad (2.18)$$

where

$Q$  = The generalized constraint force due to the supporting structure,

$Q'$  = Generalized forces due to dissipation,

$T$  = Kinetic Energy of the system.

The principle of virtual work is applied for deriving the generalized constrained force  $Q$  . The virtual work done by an applied force is given by the applied force times an arbitrary virtual displacement

$$\delta W = F \delta y \quad (2.19)$$

Note that in this case, the coordinate  $y$  is a function of the generalized coordinate and time ( i.e.  $y = f(\psi, t)$ ). Thus, virtual displacements of  $y$  can be expressed in terms of the corresponding virtual displacement of  $\psi$  by differentiating  $y$  with

res

upl

geo

and

respect to  $\psi$  while holding time fixed:

$$\delta y = \frac{\partial y}{\partial \psi} \delta \psi \quad (2.20)$$

This results in the corresponding virtual work

$$\delta W = F \frac{\partial y}{\partial \psi} \delta \psi \quad (2.21)$$

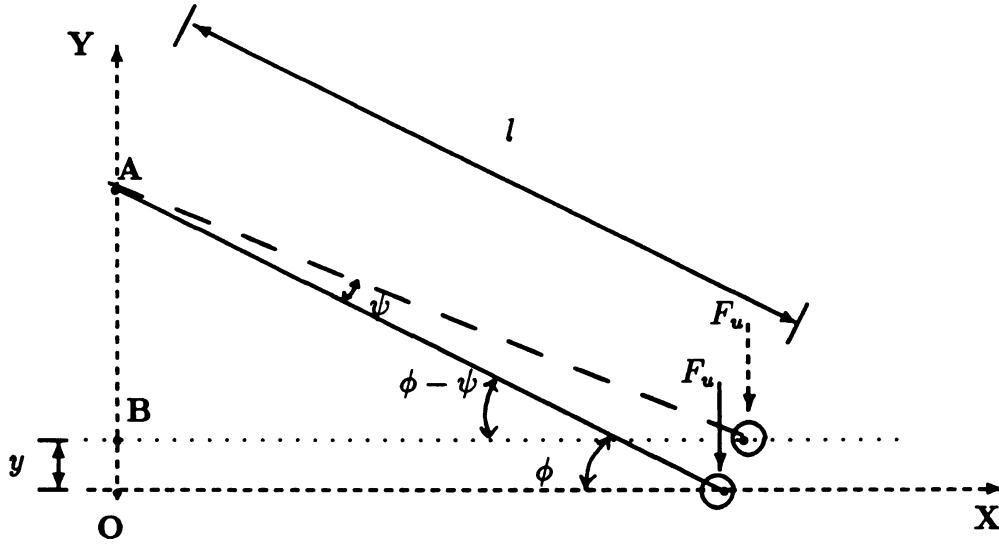


Figure 2.3: The model through the virtual displacement of the roller

Figure 2.3 presents a schematic view of the the model. Note that in this figure the upper supporting structure is replaced by a force  $F_u$  acting on the roller. From the geometry of the model, as shown in Figure 2.3, the following relationship between  $y$  and  $\psi$  is obtained

$$y = l \sin \phi - l \sin(\phi - \psi) \quad (2.22)$$



which results in the following derivative

$$\frac{\partial y}{\partial \psi} = l \cos(\phi - \psi) \quad (2.23)$$

Substituting the above in to the virtual work equation results in

$$\delta W = -F_u l \cos(\phi - \psi) \delta \psi \quad (2.24)$$

which can be written as

$$\delta W = Q \delta \psi \quad (2.25)$$

where  $Q$  is the generalized force associated with the generalized coordinate  $\psi$  and is given by

$$Q = -F_u l \cos(\phi - \psi) \quad (2.26)$$

The following expression, equation 2.5, for the kinetic energy was derived in section 2.2

$$\begin{aligned} T_{total} = & \frac{1}{2} M \{ [ r \Omega \sin \Omega t + l \sin(\phi - \psi) (\dot{\phi} - \dot{\psi}) ]^2 \\ & + [ r \Omega \cos \Omega t - \frac{1}{2} l (\dot{\phi} - \dot{\psi}) \cos(\phi - \psi) ]^2 \} \\ & + \frac{1}{2} m \{ [ r \Omega \sin \Omega t + \frac{1}{2} l \sin(\phi - \psi) (\dot{\phi} - \dot{\psi}) ]^2 \\ & + [ r \Omega \cos \Omega t - \frac{1}{2} l \cos(\phi - \psi) (\dot{\phi} - \dot{\psi}) ]^2 \} + \frac{1}{2} J_r (\dot{\phi} + \dot{\psi})^2 \end{aligned}$$

By using the above equation, the equation of motion which takes into consideration

th

M

in

v

fo

fo

on

the constraint generalized force is found by applying equation 2.19 with the following:

$$\begin{aligned} \frac{d}{dt} \left( \frac{\partial T}{\partial \dot{\psi}} \right) - \frac{\partial T}{\partial \psi} &= \frac{1}{2} m \{ -\Omega^2 r l [\sin \Omega t \cos(\phi - \psi) + \cos \Omega t \sin(\phi - \psi)] \\ &\quad - \frac{1}{2} l^2 (\ddot{\phi} - \ddot{\psi}) \} - M \{ \Omega^2 r l [\sin \Omega t \cos(\phi - \psi) \\ &\quad + \cos \Omega t \sin(\phi - \psi) + l^2 (\ddot{\phi} - \ddot{\psi}) \} + J_r (\ddot{\phi} + \ddot{\psi}) \end{aligned}$$

$$Q_u = -F_u l \cos(\phi - \psi)$$

$$Q' = -c \dot{\psi} + c \Omega + c \dot{\phi}$$

The above is non-dimensionalized by dividing both sides of the above equation by  $M l \Omega^2$ , as in section 2.2. The dimensionless form of the equation of motion which includes the generalized force is then given by:

$$\begin{aligned} &-\frac{1}{2} \alpha \xi [\sin \tau \cos(\phi - \psi) + \cos \tau \sin(\phi - \psi)] - \frac{1}{4} \alpha (\phi'' - \psi'') \\ &- \xi [\sin \tau \cos(\phi - \psi) + \cos \tau \sin(\phi - \psi)] - (\phi'' - \psi'') \\ &- \beta (\phi'' - \psi'') = -f_u \cos(\phi - \psi) + \lambda + \lambda \phi' - \lambda \psi' \end{aligned} \quad (2.27)$$

where the dimensionless parameters are described in section 2.2.

The new dimensionless parameter  $f_u$  corresponds to the dimensionless generalized force from the upper surface acting on the roller. A similar analysis can be carried out for the lower supporting structure. The dimensionless generalized constraint forces on the roller from the upper and lower structures are given by

$$f_{u/l} = \frac{F_u/l}{M l \Omega^2} \quad (2.28)$$

where  $f_l$  is the force of the lower supporting structure on the roller. It is obtained by using the same approach as above with  $F_l$  taken in the opposite direction of  $F_u$  for consistency in sign: a positive force implies compression between the relevant constraint and the roller.

The forces of the constraints on the roller at  $\psi_{max}$  and  $\psi_{min}$  are obtained by simply solving the equation of motion for  $f_{u/l}$ , yielding:

$$f_{u/l} = \frac{\mp 1}{\cos(\phi - \psi)} \left\{ -\frac{1}{2} \alpha \xi [\sin \tau \cos(\phi - \psi) + \cos \tau \sin(\phi - \psi)] \right. \\ \left. - \xi [\sin \tau \cos(\phi - \psi) + \cos \tau \sin(\phi - \psi)] - (\phi'' - \psi'') \right. \\ \left. - \frac{1}{4} \alpha (\phi'' - \psi'') + \beta (\phi'' + \psi'') - \lambda - \lambda \phi' + \lambda \psi' \right\} \quad (2.29)$$

with  $\psi = \psi_{max}$  for the "u" and  $\psi = \psi_{min}$  for the "l" subscript. Note that the "-" corresponds to the force of the upper supporting structure on the roller (i.e.  $f_u$ ) and "+" corresponds to the force of the lower supporting structure on the roller (i.e.  $f_l$ ). Based on this sign convention, whenever the force is positive, the roller may be sliding and whenever it is negative the roller cannot be sliding on the corresponding supporting structure. Thus, in order to have the roller sliding on the supporting structure,  $\psi$  must be at its maximum / minimum, and  $f_u / f_l$  must be positive, respectively.

The parameters which influence the possibility of sliding are the gap size and the bearing friction (or, equivalently, the crank speed). The gap size affects the geometry while the bearing friction (crank speed) influences the moment on the connecting rod which in turn influences the constraint force. The coefficient of restitution cannot

affect the constraint force, and hence does not play a role in determining the  $(\lambda, \rho)$  parameter regions or crank angle intervals in which sliding may occur. However, it does influence how frequently sliding actually does occur in these regions since it has a direct effect on the time required for settle-out of the impacts into a sliding motion. A set of results are presented here that demonstrates the effect of these parameters on constraint force. These results are based on the parameter set given in section 4.1.

For  $\rho = 0$ , and  $\lambda = 0$  the constraint forces possess the following symmetries: (i)  $f_u = -f_l$  and (ii)  $f_u(\theta + \pi) = -f_u(\theta)$ . For  $\rho = 0, \lambda \neq 0$  symmetry (i) holds but (ii) is broken. For  $\rho \neq 0, \lambda = 0$  symmetry (i) is broken while (ii) holds. As is demonstrated below, these facts have some interesting consequences.

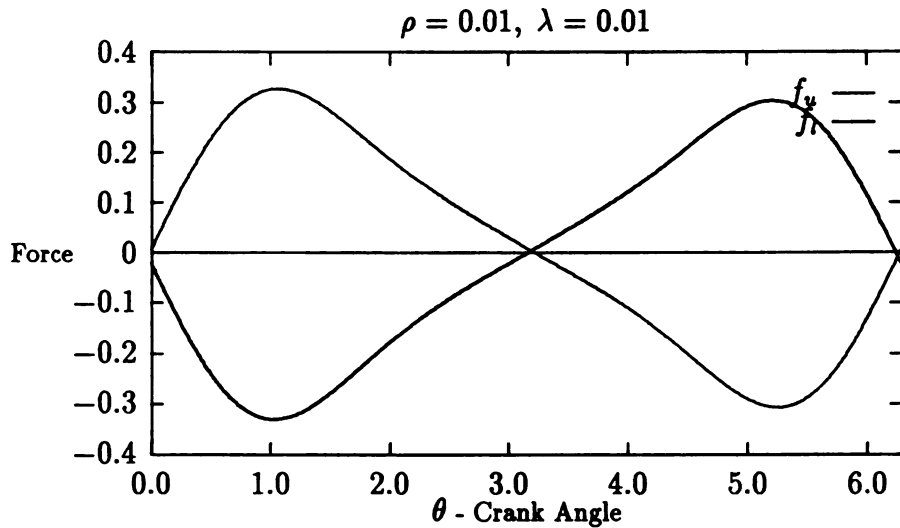


Figure 2.4: Constraint force on the roller at  $\lambda = 0.01$

Figure 2.4 presents the forces of the upper and lower supporting structures on the roller for  $\rho = 0.01$  and  $\lambda = 0.01$ . Note that, there are two crank angles at which the constraint forces change direction. From approximately 0 to  $\pi$  in crank angle the

roller may slide along the upper surface while from approximately  $\pi$  to  $2\pi$  it may slide along the lower surface.

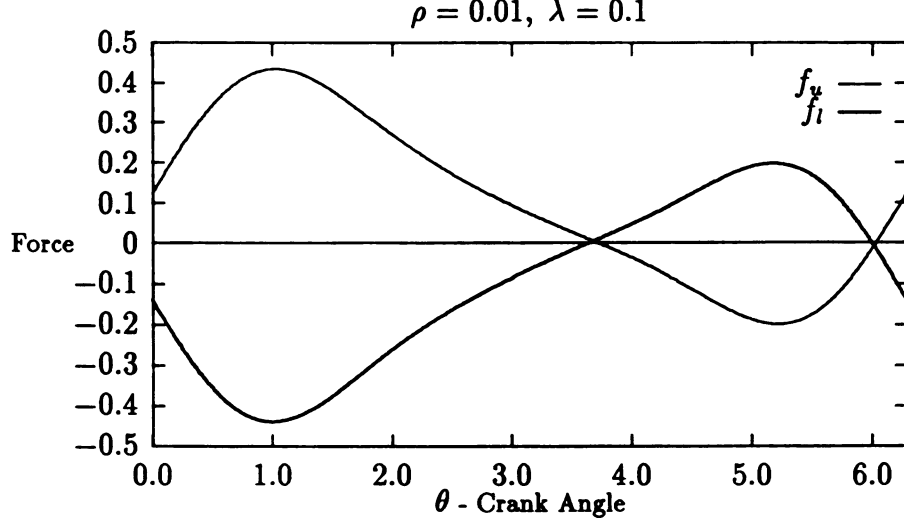


Figure 2.5: Constraint force on the roller at  $\lambda = 0.1$

Figure 2.5 shows the case with  $\rho = 0.01$  and  $\lambda = 0.1$ . As the dissipation parameter increases, the force tending to hold the roller against the upper supporting structure increases, in which case the roller can be sliding along the upper supporting structure for a longer period. Figure 2.6 demonstrates the effect of increasing the dissipation parameter to 0.25. Comparison between Figures 2.4, 2.5, and 2.6 suggests that as  $\lambda$  increases, as expected, the force of the supporting structure on the roller increases and the sliding region on the upper supporting structure is extended.

Although in the figures shown to this point it appears that  $f_u = -f_l$ , this is not the case in general. It is true only for  $\rho = 0$ . The quantity  $(f_u + f_l)$  deviates from zero as  $\rho$  is increased from zero. This lack of symmetry allows for a situation in which the roller may slide along the upper constraint over the entire crank cycle

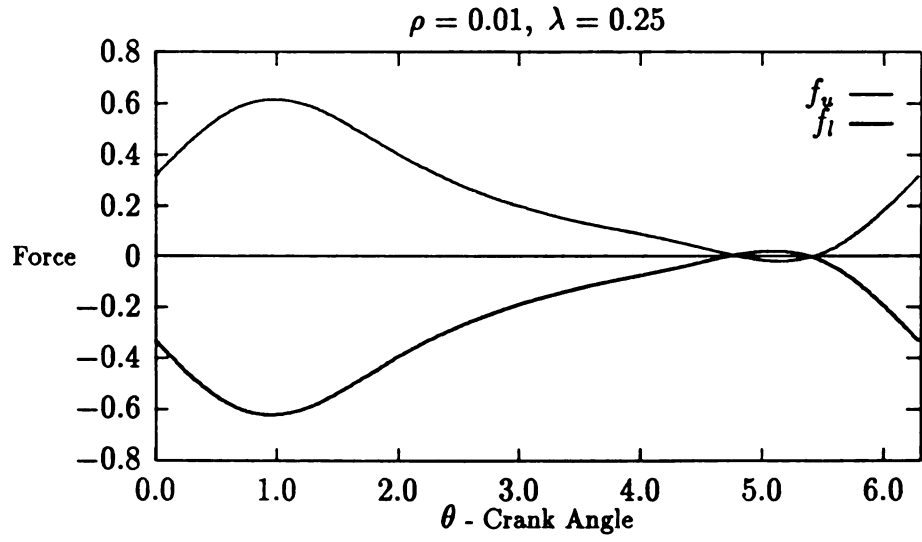


Figure 2.6: Constraint force on the roller at  $\lambda = 0.25$

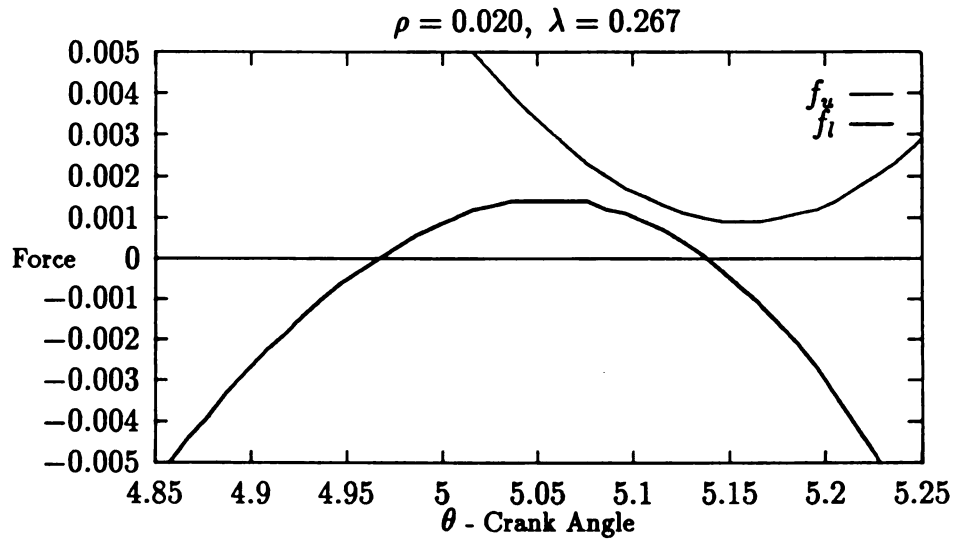


Figure 2.7: Constraint force on the roller at  $\lambda = 0.267, \rho = 0.02$

and may also slide along the lower constraint over a small crank interval. Such a case is shown in Figure 2.7 for  $\rho = 0.02$  and  $\lambda = 0.267$

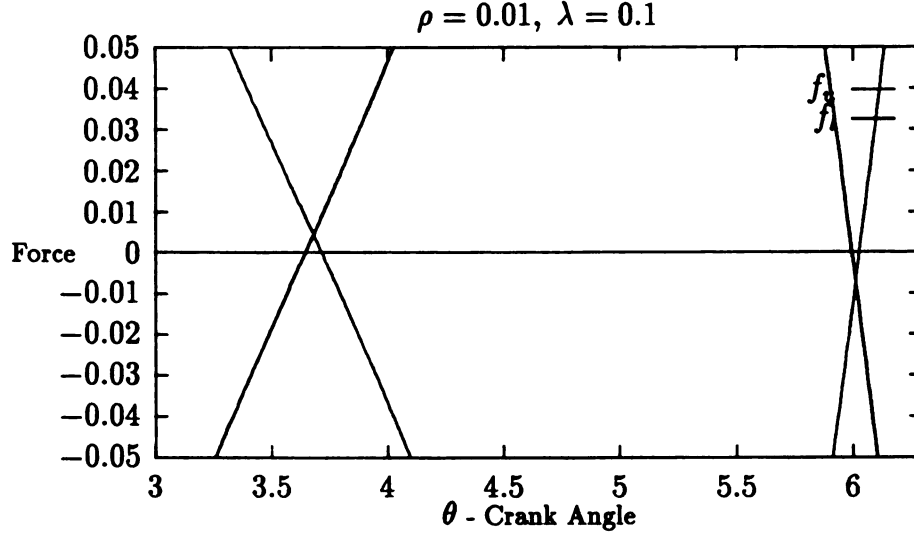


Figure 2.8: Blow up of the constraint force on the roller

The lack of symmetry also permits the existence of small crank angle intervals over which sliding may occur on either the upper or the lower structure. Figure 2.7 clearly shows such a interval in the range  $4.96 < \theta < 5.14$ . A similar situation occurs near the leftmost crossing point (i.e., the continuation of the crossing at  $\theta = \pi$  for  $\rho = \lambda = 0$ ) of  $f_u$  and  $f_l$  for all values of  $\rho$  and  $\lambda$  for which crossings occur. Similarly, near the second crossing point (the continuation of the one originating at  $\theta = 2\pi$  for  $\rho = \lambda = 0$ ), there exists an interval over which sliding cannot occur along either constraint. Figure 2.8 shows a blow up of the case from Figure 2.5 ( $\lambda = 0.1, \rho = 0.01$ ) which clearly shows these regions. These intervals are typically small and for small  $\rho$  do not have a significant effect on the dynamics of the system.

Figure 2.9 represents the results of having very large friction at the joint (or low



1  
U  
C  
SC  
ST  
RA

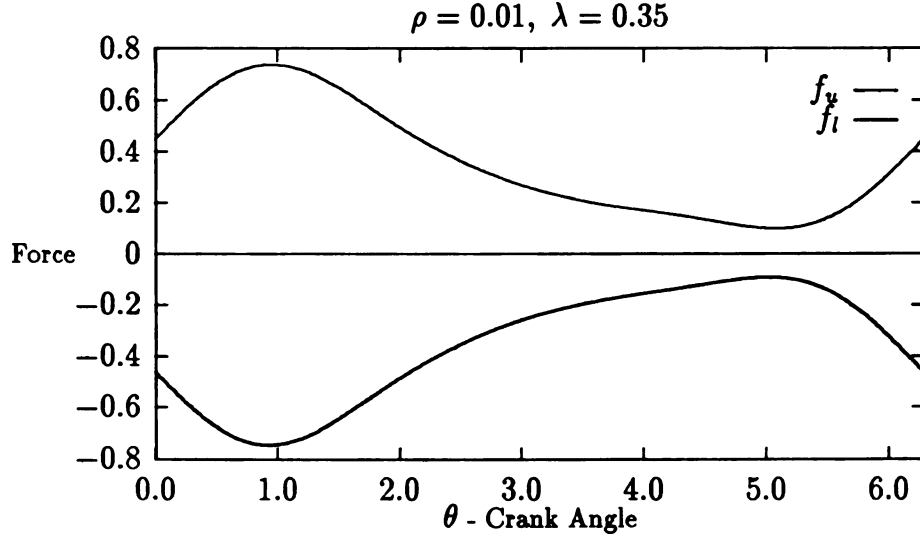


Figure 2.9: Constraint force on the roller at  $\lambda = 0.35$

speed),  $\lambda = 0.35$ . Here the roller may slide along the upper supporting structure throughout the entire crank cycle. Note that in this situation, if started in a sliding mode of motion, the roller will remain sliding along the upper surface and will never release.

Figure 2.10 presents an overview of the effect of the gap size and the dissipation coefficient on the sliding of the roller on the upper and lower supporting structures. Region *I* corresponds to the parameter ranges where there can be sliding on both parts of the supporting structure during one cycle, for example, as shown in Figures 2.4, 2.5, and 2.6. Region *II* represents the parameter range in which the roller can be sliding on the upper supporting structure during the entire cycle and there is some interval in each cycle for which the roller can also slide on the lower supporting structure, for example, as shown in Figure 2.7. Finally, region *III* corresponds to the range of parameters for which the roller can slide on the upper surface over the entire

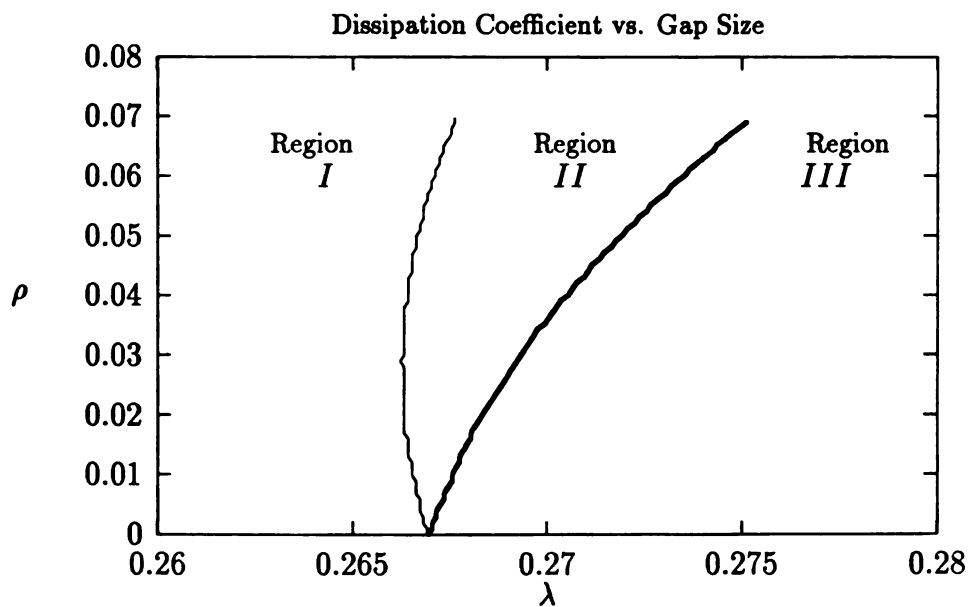


Figure 2.10: Regions of Sliding on the Supporting Structure.

crank cycle and nowhere can it slide in contact with the lower surface, for example,

Figure 2.9.

# Chapter 3

## Methods of Analysis

In this chapter, three methods for presenting the results obtained from the equations of motion, equation 2.13 and equation 2.17, are described. First, the concept of a Poincare map is introduced as a geometrical means of presenting simulation data. Next, a statistical analysis which presents the average number of impacts and the associated impact velocities along locations of the supporting structure is described. This method of presentation provides information regarding possible patterns of wear in the cylinder. Finally, impact spectra are defined that provide information regarding the number of impacts and the associated impact velocities as a function of the crank angle. This is essentially a polar representation of the statistical analysis.

### 3.1 Poincare Section

An important conceptual tool for understanding the behavior of a time periodic system is the Poincare map. Typically this map is defined to sample the system's

displa

period

tem i

T

in sec

when

.

tion

is a

wh

th

in

as

displacement and velocity, or, more generally, its dynamics state variables, once per period of the excitation. Using such a map, a continuous-time non-autonomous system is reduced to a discrete-time system with one less dimension.

The linearized and dimensionless equation of motion, equation 2.13, was obtained in section 2.2, and is restated here:

$$a \psi'' + b \psi' + c(\tau)\psi = f(\tau)$$

where  $c(\tau)$ , and  $f(\tau)$  are all periodic in  $\tau$  with period  $2\pi$ .

Note that this equation is valid for  $\psi_{min} \leq \psi \leq \psi_{max}$ . Also, based on the assumptions given section 2.1, whenever  $\psi = \psi_{max}$  or  $\psi = \psi_{min}$  the simple impact rule [24] is applied (i.e. equation 2.17) which results in a jump in velocity given by:

$$\dot{\psi}_{after} = (1 + e) \left[ \frac{\xi^2 \sin \tau \cos \tau}{\Lambda^2} \psi \right] - e \dot{\psi}_{before}$$

where  $e$  is a coefficient of restitution with a value between zero and unity. Note that the above equations completely determine the dynamics of the system.

To define the Poincare section for this system, we first write the equation of motion in the form of a first order system of equations with  $(\psi, \dot{\psi}, \tau(\text{mod}2\pi)) = (x_1, x_2, \theta)$  as follows:

$$x_1' = x_2 \tag{3.1}$$

$$x_2' = -\frac{b}{a}x_2 - \frac{c(\theta)}{a}x_1 + \frac{f(\theta)}{a} \tag{3.2}$$

where

sect

In t

time

take

a

c

$$\theta' = 1 \quad (3.3)$$

where  $(\quad)'$  corresponds to the dimensionless time derivative (as described in section 2.3 ).

The three variables,  $(x_1, x_2, \theta)$ , are required for specifying the state of the system.

In this three-dimensional phase space, solutions are restricted to

$\psi_{min} \leq x_1 \leq \psi_{max}$ . The time variable is taken to be the crank angle so that it takes on values between 0 and  $2\pi$ , i.e.  $0 \leq \theta \leq 2\pi$ .

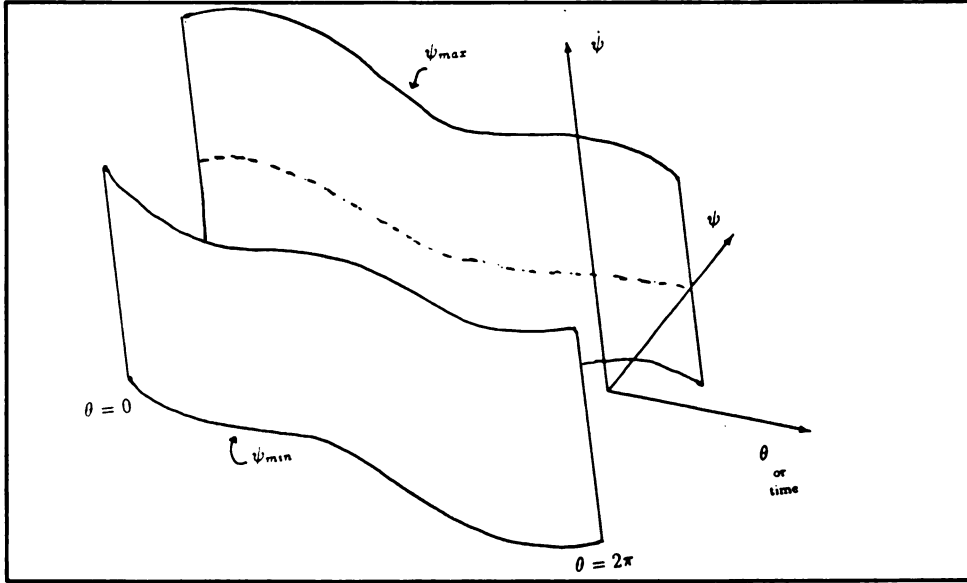


Figure 3.1: Three Dimensional phase space, with the restriction

Figure 3.1 illustrates the three dimensional extended phase space  $(\psi, \dot{\psi}, \tau)$  and its restrictions for the present system. It can be seen that a Poincare section is conveniently defined in this case using the surface of  $\psi_{max}$  or  $\psi_{min}$  in the three



dimensional space. The Poincare section for this system is thus defined as

$$\Sigma = \{(x_1, x_2, \theta) \mid x_1 = \psi_{max}, x_2 > 0\} \quad (3.4)$$

The Poincare' map  $P$  is a rule that takes points in  $\Sigma$  back into  $\Sigma$  under the action of the equation of motion. It can be represented as

$$P : \Sigma \rightarrow \Sigma, \text{ or, } (x_{2i+1}, \theta_{i+1}) = P(x_{2i}, \theta_i) \quad (3.5)$$

where the points  $(x_{2i}, \theta_i)$  are in  $\Sigma$ . Note that points in  $\Sigma$  correspond to the velocity of the roller as it is just coming in to contact with the constraint at  $\psi = x_1 = \psi_{max}$  at the  $i$ th impact, that is  $x_{2i} = \dot{\psi}_i$ , and the crank angle at which the impact occurs,  $\theta_i$ .

The map  $P$  simply relates points between successive impacts in an implicit functional form. The map can not be written in closed form for this system and will be generated by directly sampling the points as defined during simulations. Similar maps have been used in the investigations of other impacting systems and are known to possess interesting singular behavior (see Shaw [3], Shaw and Holmes [4], Karagiannis [13], Whiston [22], and Pfeiffer and Kunert [14]).

## 3.2 Impact Distribution Profile

The following approach is taken for performing the statistical analysis. We define the domain of the possible dimensionless impact locations on the supporting structure as

$D = [1 - \xi, 1 + \xi]$ , and the coordinate  $x$  as the location of an impact measured such that  $x = 1$  corresponds to the mid point of  $D$ . Thus  $x \in D$ . Note that  $x = 1 - \xi$  corresponds to the crank angles  $\theta = (2n + 1)\pi$  (for  $n = 0, \pm 1, \pm 2, \dots$ ) and  $x = 1 + \xi$  corresponds to the crank angles  $\theta = 2n\pi$  (for  $n = 0, \pm 1, \pm 2, \dots$ ).

The domain  $D$  is subdivided into  $j$  equal subintervals of width  $\Delta x = \frac{2\xi}{j}$ , designated as  $\Delta x_i, i = 1, 2, \dots, j$ . In each  $\Delta x_i$ , there will be  $N_i$  impacts during  $n$  crank rotations. The total number of impacts during this time is given by  $N = \sum_{i=1}^j N_i$ .

We designate the impact velocities over this period according to their impact location by labeling them as  $\dot{\psi}_k(\Delta x_i)$ ,  $k = 1, 2, \dots, N_i$ . Based on this, we can compute an average impact velocity for each interval  $\Delta x_i$  as

$$\langle \dot{\psi}(\Delta x_i) \rangle = \frac{\sum_{k=1}^{N_i} \dot{\psi}_k(\Delta x_i)}{N} \quad i = 1, 2, \dots, j \quad (3.6)$$

Bar graphs of  $\langle \dot{\psi}(\Delta x_i) \rangle$  versus  $\Delta x_i$  for  $i = 1, 2, \dots, j$  provide a measure of the number of impacts and their severity, given by the impact velocity, versus the dimensionless location of the impact on the supporting structure. It is worth noting that this distribution is the product of the average impact velocity in each  $\Delta x_i$  and the fraction of impacts which occur in each  $\Delta x_i$ , that is  $\frac{N_i}{N}$ . If  $\psi$  is a stationary process, then as  $N \rightarrow \infty$  these graphs will converge on to a limiting distribution. These plots provide useful information regarding possible locations of wear, heat generation, noise generation, and fatigue due to repetitive impacts. They will be referred to as impact profiles or impact distribution profiles. In these diagrams average impact velocities on the upper supporting structure are shown with positive

sign while those on the lower supporting structure are shown with a negative sign. In this manner a single diagram can capture the entire impact distribution.

### 3.3 Impact Spectra

Impact spectra provide information relating the number and severity of impacts to the crank angle. Note that impact spectra are a polar representation of the data defined in the previous section. Here we define the domain as  $D = [0, 2\pi)$ . We subdivide the domain into  $j$  equal subinterval of width  $\Delta\theta$ , labeled as  $\Delta\theta_i, i = 1, 2, \dots, j$ . Let  $N_i$  be the number of impacts which occur in  $\Delta\theta_i$  in  $n$  revolutions of the crank and let  $N = \sum_{i=1}^j N_i$  be the total number of impacts. Here the impact velocities are labeled according to the crank angle at impact as  $\dot{\psi}_k(\Delta\theta_i), k = 1, 2, \dots, N_i$ . Based on this, we compute an average velocity for each interval  $\Delta\theta_i$  as

$$\langle \dot{\psi}(\Delta\theta_i) \rangle = \frac{\sum_{k=1}^{N_i} \dot{\psi}_k(\Delta\theta_i)}{N} \quad (3.7)$$

This polar representation of the impact velocity provides useful information relating the impacts and the corresponding crank angles. Note that separate spectra figures must be produced for impacts on the upper and lower supporting structure.

# Chapter 4

## Results

### 4.1 Introduction

In this chapter we present results from simulations. Results are presented in various forms: simple time traces ( $\psi$  vs.  $t$ ), phase planes ( $\dot{\psi}$  vs.  $\psi$ ), Poincare maps, impact distribution profiles, and impact spectra. We emphasize the use of impact distribution profiles since these are the most relevant to the practical issues of wear.

Some general observations for a typical chaotic response are given first, and then these are followed by sets of simulations which describe some general behaviors which are observed as the gap size,  $\rho$ , the dissipation parameter,  $\lambda$ , and the coefficient of restitution,  $e$ , are varied. These results are grouped into three sets. The first is for parameter ranges where sliding is not observed during the steady state response, this range is for small values of  $\lambda$  ( $\lambda \ll 1$ ) and  $e$  values slightly less than unity ( $(1 - e) \ll 1$ ). The second set of simulations is also for  $e$  near unity, but  $\lambda$  values are large enough so that sliding occurs during the steady state motion. The final set

of simulations is carried for fixed  $\rho$  and  $\lambda$ , with  $e$  decreasing. This set indicates the general trend observed as the impacts become more dissipative.

In the simulations three general types of responses are observed. The simplest type of response is periodic, in which impact patterns are repeated and the motion is regular. The second type of motion is ultimately periodic, but experiences “transient chaos”. This occurs when chaos is observed over a significant period well beyond what would be typically considered as transient, and the motion then transits into a periodic pattern, in which it remains thereafter. The last type of response is chaos which is sustained over at least 1000 crank cycles. Each of these three types are observed in sliding and non-sliding cases, although periodic motions are more prevalent when sliding occurs.

Typical values for a slider-crank in an automotive four-cylinder gasoline engine, taken from a particular Ford Motor Company engine [12], are used in this study. They are

$$m = 0.00399 \text{ lb. sec.}^2 \text{ in.}^{-1}$$

$$M = 0.00210 \text{ lb. sec.}^2 \text{ in.}^{-1}$$

$$r = 1.6535 \text{ in.}$$

$$l = 5.4570 \text{ in.}$$

$$I_r = 0.0295 \text{ lb. sec.}^2 \text{ in.}$$

which result in the following dimensionless parameter values

$$\xi = 0.3030$$

$$\alpha = 1.9000$$

$$\beta = 0.4719$$

Note that throughout this investigation, these values are kept constant and the study is performed based on varying the values of the dissipation parameter,  $\lambda$ , the gap size,  $\rho$ , and the coefficient of restitution,  $e$ .

## 4.2 General Observation of Chaotic Motion

Figure 4.1 represents a time trace of the steady state behavior of the system (i.e.  $\psi$  vs.  $\tau$ ) for two crank cycles, for parameter values  $\lambda = 0.05$ ,  $\rho = 0.01$ , and  $e = 0.9$ , obtained after 25 cycles during which transients have decayed. Note that, while certain patterns are repeated, no strict periodicity is observed in this figure. In fact, the system has a chaotic response to the periodic excitation provided by the crank. Also, note that from this figure it is explicitly seen that  $\psi$  is constrained by  $\psi_{max}$  and  $\psi_{min}$ . Figure 4.2 shows the phase portrait ( $\dot{\psi}$  vs.  $\psi$ ) of the system for the same two cycles of the crankshaft with the same parameters. A Poincare plot of the system showing points corresponding to the absolute velocity before impact at the top side of the cylinder and the crank angle at impact is presented in Figure 4.3. This plot, taken over 3000 crank revolutions, clearly demonstrates the chaotic behavior of

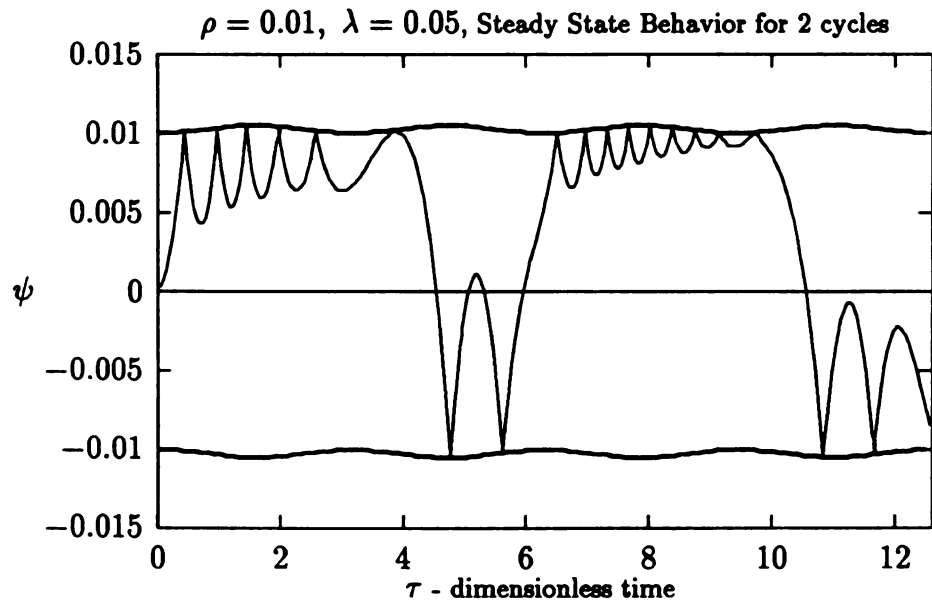


Figure 4.1: Time Trace

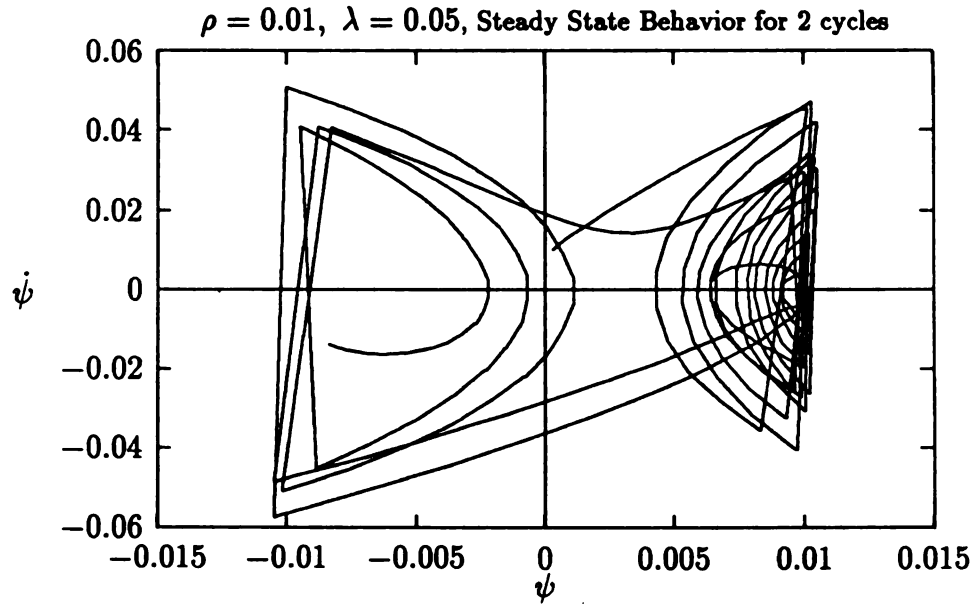


Figure 4.2: Phase Portrait

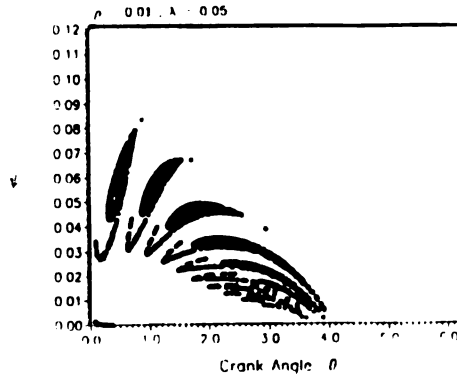


Figure 4.3: Poincare Map,  $\lambda = 0.05$  and  $\rho = 0.01$

the system. During an initial transient period, the points from the map appear to be randomly placed. However, as more data points are taken the highly ordered pattern shown is formed. Figure 4.4 and Figure 4.5 contain two consecutive magnifications of the Poincare plot (Figure 4.3) which demonstrate the fractal nature of this chaotic attractor (Moon [26]).

An interesting feature of this strange attractor is that it is composed of several "lobes", some of which are distinct but others of which conjugate near zero velocity. These lobes are correlated to the physical motion in the following way: A series of impacts occur which has points in these lobes moving sequentially from the upper left to the lower right. This corresponds to a simple sequence of impacts which occur as the crank advances and for which the impact velocity being reduced at each impact. Eventually the moment acting on the connecting rod reverses sign, and it is released from this sequence for some time. As the time trace of Figure 4.1 shows, there is some pattern to the motion and although is not periodic, certain features are repeated each crank cycle. This results in the observed structure of the Poincare map.



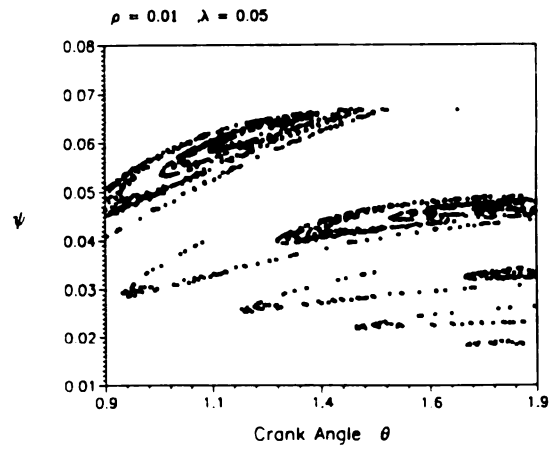


Figure 4.4: First Magnification of Poincare Map

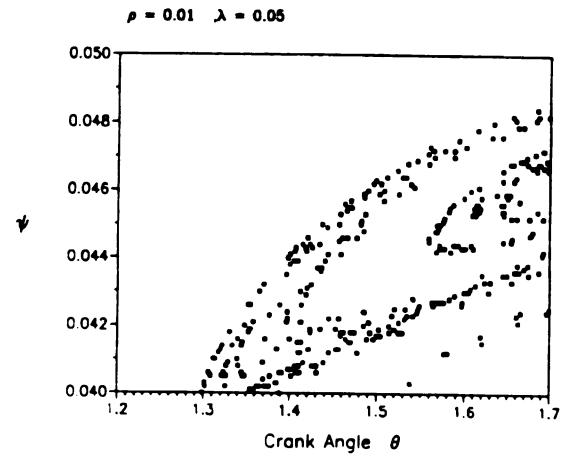


Figure 4.5: Second Magnification of Poincare Map

### 4.3 Non-sliding Dynamics

For the simulations presented in this section, we keep the coefficient of restitution,  $e$ , fixed at a value of 0.9 and carry out simulations for the  $3 \times 3$  parameter matrix with  $\lambda = 0.025, 0.05, 0.075$  and  $\rho = 0.01, 0.015, 0.2$ . The results are depicted in the form of impact distribution patterns and are presented in Figures 4.6 - 4.14. It is noted that all three types of response occur. The cases  $(\lambda, \rho) = (0.025, 0.01), (0.025, 0.015)$ , and  $(0.075, 0.01)$  exhibit transient chaos (i.e., Figures 4.6, 4.7, and 4.12), cases  $(\lambda, \rho) = (0.025, 0.02), (0.05, 0.01), (0.05, 0.02), (0.075, 0.015)$ , and  $(0.075, 0.02)$  (i.e., Figures 4.8, 4.9, 4.11, 4.13, and 4.14) exhibit sustained chaos, and case  $(\lambda, \rho) = (0.05, 0.015)$  (i.e., Figure 4.10) is periodic without a chaotic transient. The impact distribution patterns reflect these facts in the following way: chaos results in a widely distributed set of impacts, periodicity is reflected by clean spikes, and transient chaos is dominated by spikes but has superimposed some more uniformly distributed impacts whose level depends on the duration of the chaos in relation to the duration of the total data sample. As the sample length is increased, this background will decrease in amplitude.

We show Poincare maps and impact spectra for three cases that represent the three types of motions:  $(\lambda, \rho) = (0.05, 0.015)$  for periodic motion, see Figures 4.18, 4.19, and 4.20;  $(\lambda, \rho) = (0.025, 0.01)$  for transient chaos, see Figures 4.15, 4.16, and 4.17; and  $(\lambda, \rho) = (0.075, 0.02)$  for sustained chaos, see Figures 4.21, 4.22, and 4.23. A comparison of the Poincare maps, impact spectra, and impact distribution patterns for these cases indicates the sufficiency of the impact distribution for characterizing

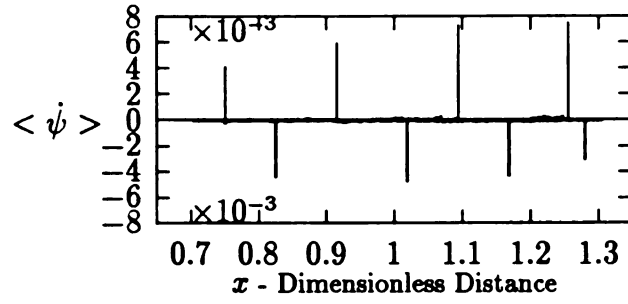


Figure 4.6: Impact Distribution Pattern,  $\lambda = 0.025$  and  $\rho = 0.010$

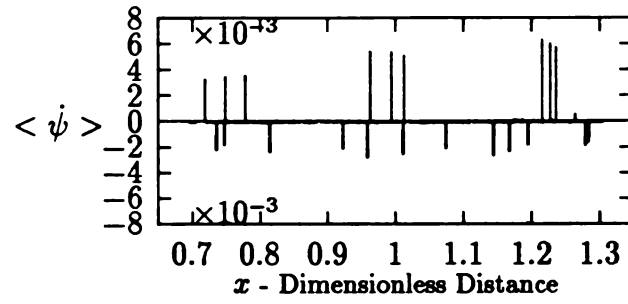


Figure 4.7: Impact Distribution Pattern,  $\lambda = 0.025$  and  $\rho = 0.015$

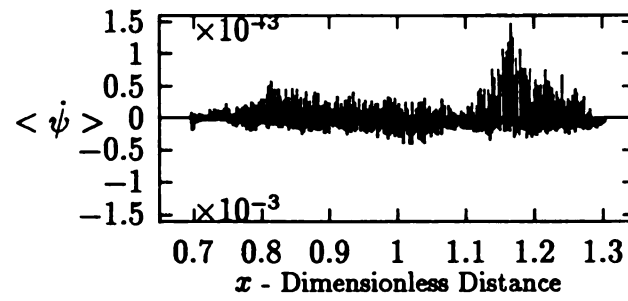


Figure 4.8: Impact Distribution Pattern,  $\lambda = 0.025$  and  $\rho = 0.020$

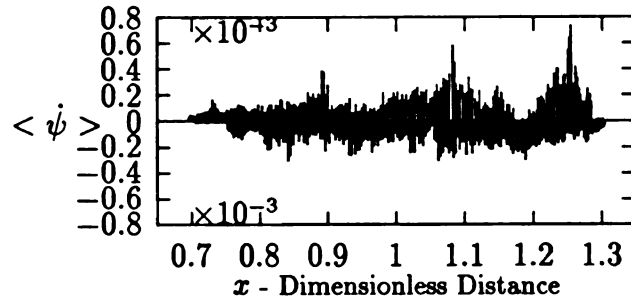


Figure 4.9: Impact Distribution Pattern,  $\lambda = 0.05$  and  $\rho = 0.010$

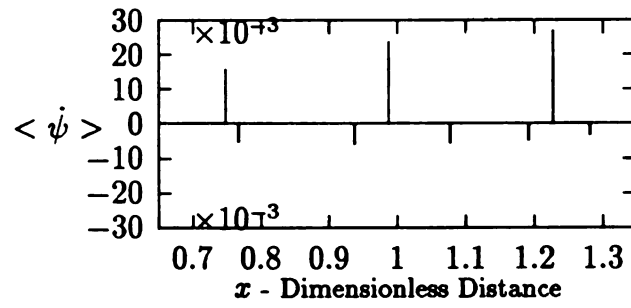


Figure 4.10: Impact Distribution Pattern,  $\lambda = 0.05$  and  $\rho = 0.015$

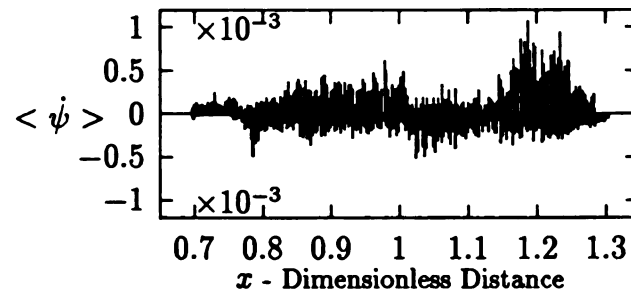


Figure 4.11: Impact Distribution Pattern,  $\lambda = 0.05$  and  $\rho = 0.020$

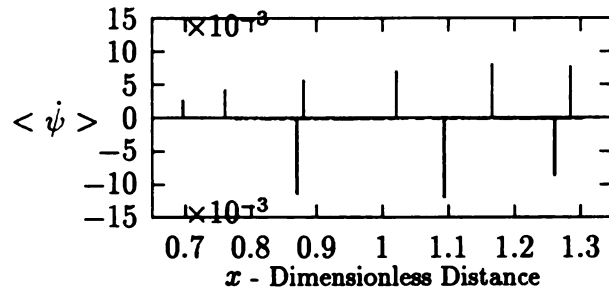


Figure 4.12: Impact Distribution Pattern,  $\lambda = 0.075$  and  $\rho = 0.010$

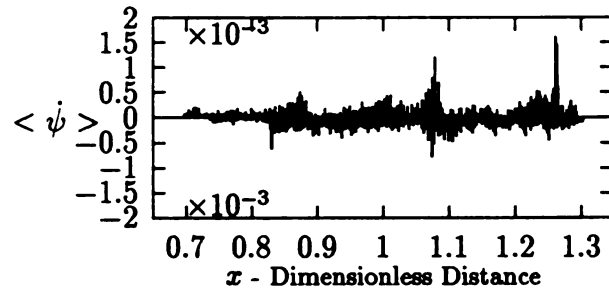


Figure 4.13: Impact Distribution Pattern,  $\lambda = 0.075$  and  $\rho = 0.015$

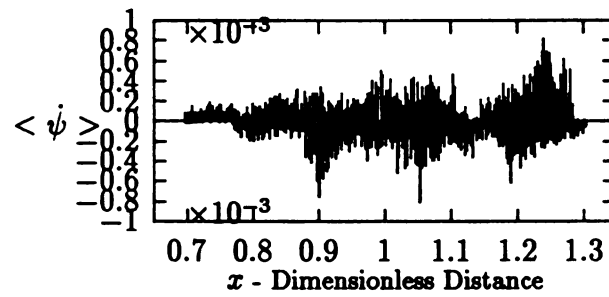


Figure 4.14: Impact Distribution Pattern,  $\lambda = 0.075$  and  $\rho = 0.020$

the response of the system.

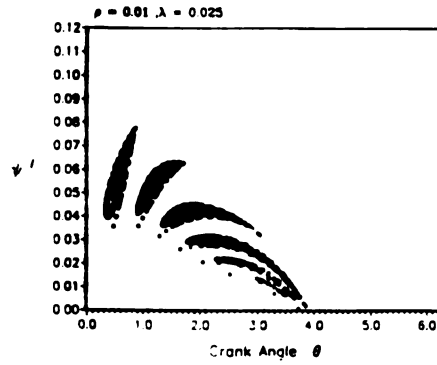


Figure 4.15: Poincare Map,  $\lambda = 0.025$  and  $\rho = 0.01$

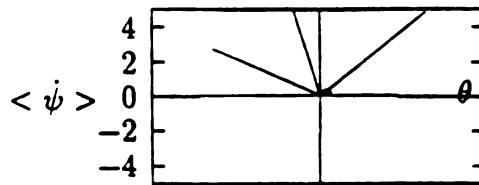


Figure 4.16: Impact Spectra. Upper Wall  $\lambda = 0.025$  and  $\rho = 0.01$

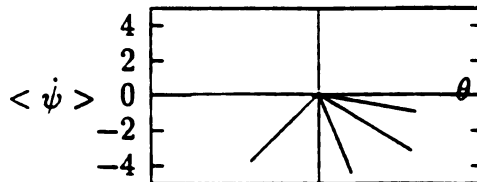


Figure 4.17: Impact Spectra. Lower Wall  $\lambda = 0.025$  and  $\rho = 0.01$

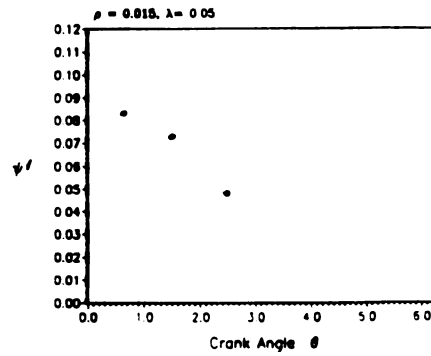


Figure 4.18: Poincare Map,  $\lambda = 0.05$  and  $\rho = 0.015$

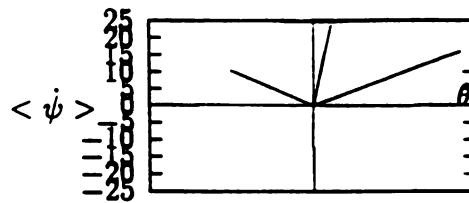


Figure 4.19: Impact Spectra, Upper Wall  $\lambda = 0.05$  and  $\rho = 0.015$

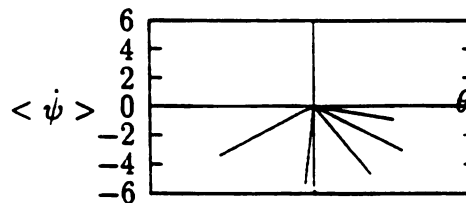


Figure 4.20: Impact Spectra, Lower Wall  $\lambda = 0.05$  and  $\rho = 0.015$

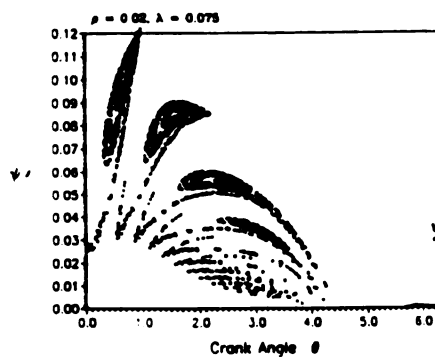


Figure 4.21: Poincare Map,  $\lambda = 0.075$  and  $\rho = 0.02$

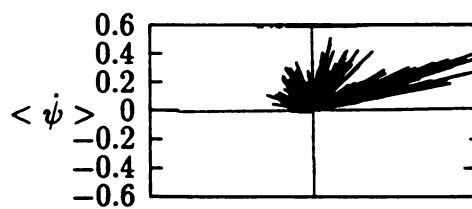


Figure 4.22: Impact Spectra, Upper Wall  $\lambda = 0.075$  and  $\rho = 0.02$

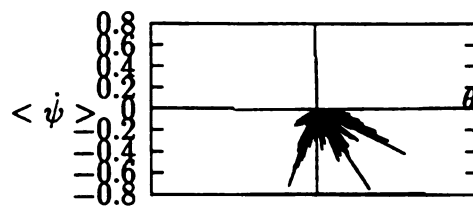


Figure 4.23: Impact Spectra, Lower Wall  $\lambda = 0.075$  and  $\rho = 0.02$



The following observation can be made based on the impact distribution patterns shown in Figures 4.6 - 4.14. Chaotic motions lead to a quite uniform spreading of the impacts over a range of locations while periodic motions lead to highly localized impact locations. Also, as a general rule, the average impact velocities increase as the gap size is increased. This is expected since the free motion has a longer time in which to build up momentum before impact.

Also note that, as expected, the impact velocities are greater on the upper constraint than on the lower. Also, this difference increases as  $\lambda$  is increased. This is due to the increase of the moment acting on the connecting rod from the bearing, and in particular from the  $\lambda (\dot{\theta} + \dot{\phi})$  term which is biased by the rotation direction. In all cases, there are regions in which very small impact velocities occur (this is most directly seen by considering the Poincare maps). These small impact velocities will result, as  $\lambda$  increased or  $e$  is decreased, in motions in which sliding occurs during some part of the cycle.

Another point worth noting is that there is no apparent correspondence relating the parameter variation to specific trends in the types of motion observed (at least in this parameter range). Chaos and periodicity occur for  $(\lambda, \rho)$  values without rhyme or reason. In fact, for the periodic motions observed, very slight changes in the parameters rendered the motion chaotic. It is therefore impossible to draw substantive conclusions regarding non-sliding motions, other than the general observations given above. In addition, *a priori* prediction of the nature of the response at a given set of parameters is impossible. One must simply run the simulation to determine the steady state motion.

## 4.4 Dynamics Involving Sliding

In the simulation routine, the appearance of an extremely low relative velocity at impact is assumed to initiate sliding. At such a point the simulation program simply advances the crank angle to the release value and starts the free flight conditions at  $\psi(\theta) = \psi_{max}(\theta)$  (or  $\psi(\theta) = \psi_{min}(\theta)$ , respectively) and  $\dot{\psi}(\theta) = \dot{\psi}_{max}(\theta)$  (or  $\dot{\psi}(\theta) = \dot{\psi}_{min}(\theta)$ , respectively) with  $\theta$  set at the release value. Details of these algorithms are given in Appendix B.

In these simulations  $e$  is again fixed at 0.9 and a  $3 \times 3$  matrix of  $(\lambda, \rho)$  values is considered with  $\lambda = 0.15, 0.20, 0.25$  and  $\rho = 0.010, 0.015, 0.020$ . Note that the  $\lambda$  values are larger here, corresponding to values where sliding occurs during some part of the motion. Again the results are presented in the form of impact distribution diagrams given in Figures 4.24 - 4.32. Periodic motions are much more prevalent as  $\lambda$  is increased in this parameter range. This is quite simply due to the fact that in general dissipation tends to discourage chaos.

As in the case of non-sliding motions, an increase in the gap size results in larger impact velocities and increases in  $\lambda$  tend to increase the difference between the impact velocity magnitudes on the upper supporting structure and the lower supporting structure. Increases in  $\lambda$  also tend to suppress chaotic dynamics. This can be seen in the impact distribution patterns provided in this section (Figures 4.24 - 4.32).

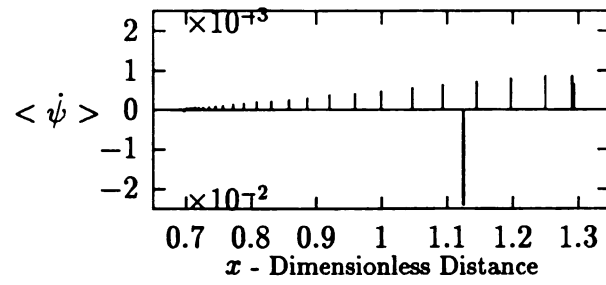


Figure 4.24: Impact Distribution Pattern,  $\lambda = 0.15$  and  $\rho = 0.010$

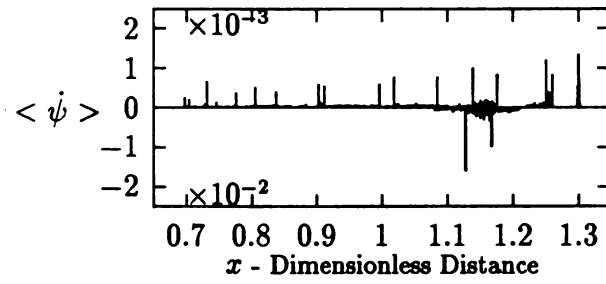


Figure 4.25: Impact Distribution Pattern,  $\lambda = 0.15$  and  $\rho = 0.015$

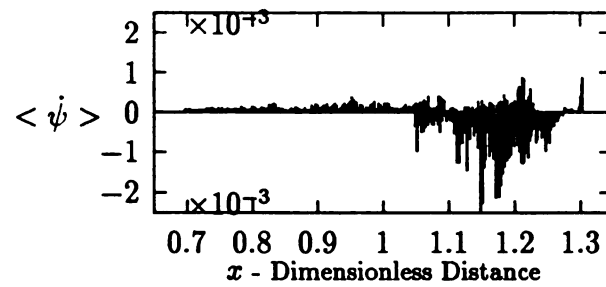


Figure 4.26: Impact Distribution Pattern,  $\lambda = 0.15$  and  $\rho = 0.020$

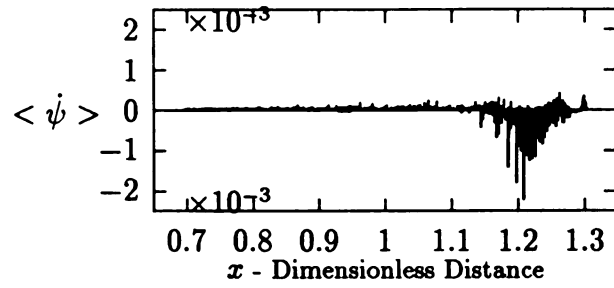


Figure 4.27: Impact Distribution Pattern,  $\lambda = 0.20$  and  $\rho = 0.010$

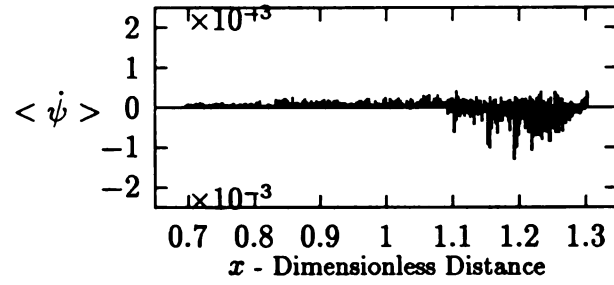


Figure 4.28: Impact Distribution Pattern,  $\lambda = 0.20$  and  $\rho = 0.015$

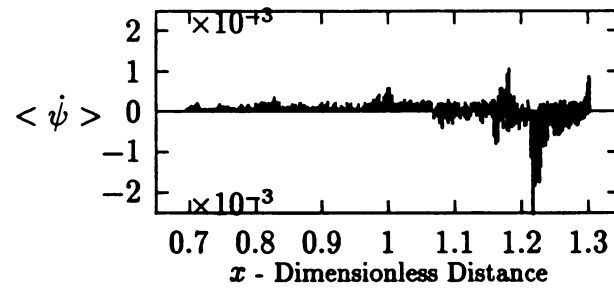


Figure 4.29: Impact Distribution Pattern,  $\lambda = 0.20$  and  $\rho = 0.020$

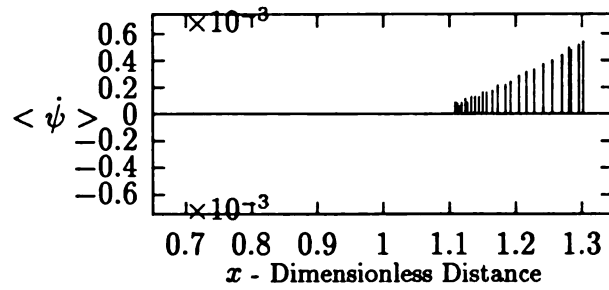


Figure 4.30: Impact Distribution Pattern,  $\lambda = 0.25$  and  $\rho = 0.010$

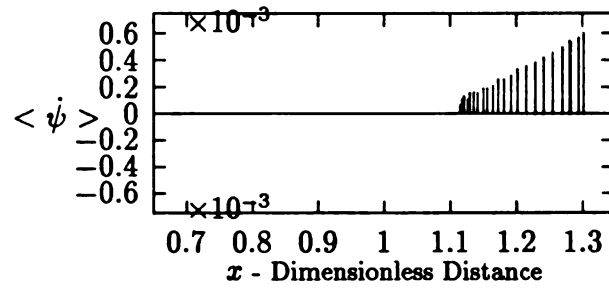


Figure 4.31: Impact Distribution Pattern,  $\lambda = 0.25$  and  $\rho = 0.015$

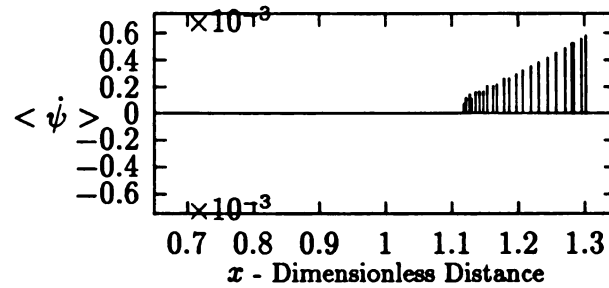


Figure 4.32: Impact Distribution Pattern,  $\lambda = 0.25$  and  $\rho = 0.020$

Figures 4.33 and 4.34 present the two Poincare maps for  $\rho = 0.015$ , with  $\lambda = 0.2$  and  $0.25$ . At  $\lambda = 0.2$  the motion is chaotic. During this chaotic motion, sliding occurs intermediately, but not infrequently. As  $\lambda$  is increased, at approximately  $\lambda = 0.22$  only transient chaos is observed, and for  $\lambda = 0.23$  and above, simple periodic motion occurs. The case of  $\lambda = 0.25$  indicates that these periodic motions involve cycles of low velocity impacts concluding in sliding, and then release. A time trace

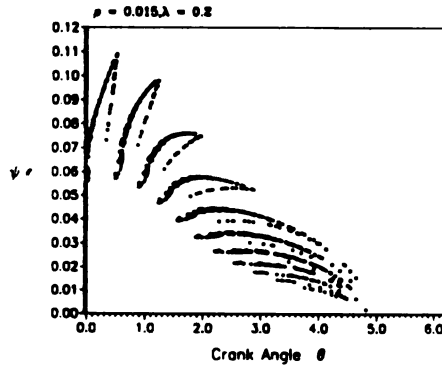


Figure 4.33: Poincare Map,  $\lambda = 0.2$  and  $\rho = 0.015$

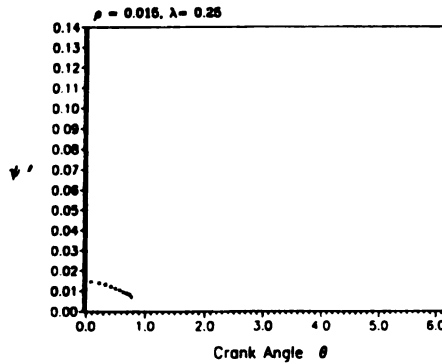


Figure 4.34: Poincare Map,  $\lambda = 0.25$  and  $\rho = 0.015$

for the case of  $(\lambda, \rho) = (0.25, 0.015)$  is shown in figure 4.35. Note that this is shown for three crank cycles and the response is periodic.

Note that in the case of relatively large values of the dissipation coefficient  $\lambda$ , unlike the case of lower values of  $\lambda$ , the response of the system does not change

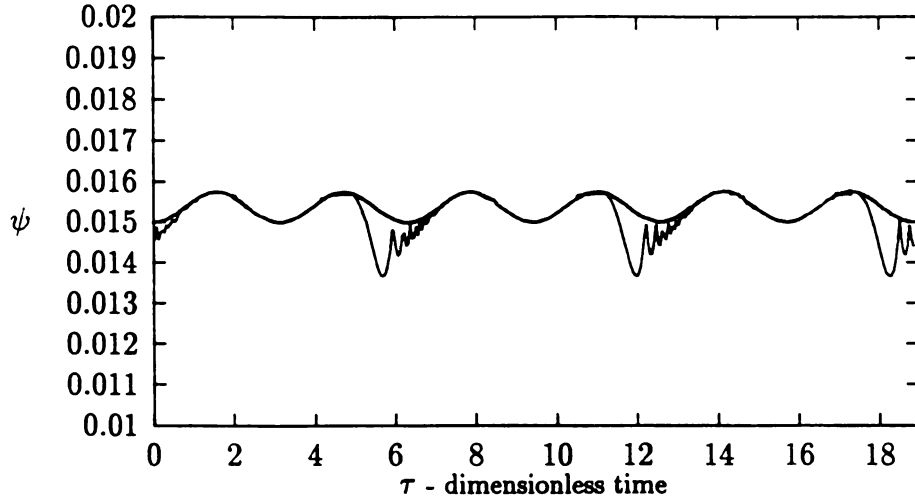


Figure 4.35: Time Trace,  $e = 0.9$ ,  $\lambda = 0.25$ , and  $\rho = 0.015$

from periodic to chaotic with small variations of  $\rho$ . In the previous section it is seen that with the slightest change of the gap size at a fixed  $\lambda$ , the response changes from periodic to chaotic, while in the case of high  $\lambda$ , if the response is periodic, small variations of the gap size do not affect the periodicity. This can be seen in Figures 4.36, 4.34, and 4.37.

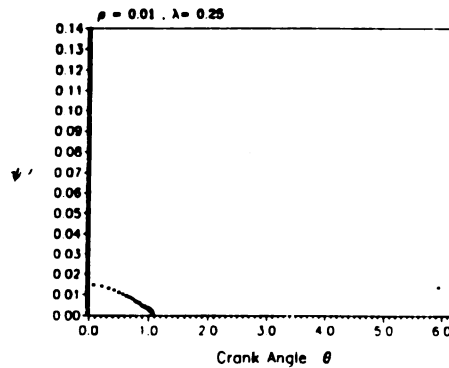


Figure 4.36: Poincare Map,  $\lambda = 0.25$  and  $\rho = 0.01$

Note that at the highest dissipation coefficient used in this study,  $\lambda = 0.25$ ,

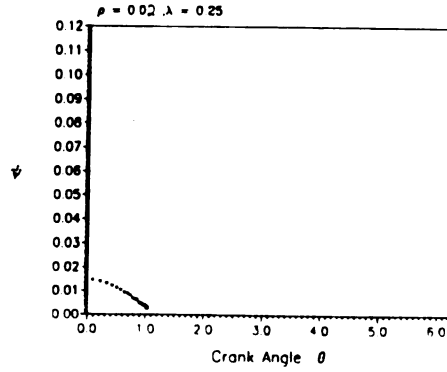


Figure 4.37: Poincare Map,  $\lambda = 0.25$  and  $\rho = 0.02$

there are no impacts on the lower supporting structure. Comparison of these impact distribution patterns with the ones presented in the previous section suggest that as  $\lambda$  increases the locations of the impacts on the lower supporting structure become more limited and the impacts on the lower supporting structure become more severe. Note that the impact locations shift toward the end of the supporting structure (i.e. head of the cylinder) and for  $\lambda$  above 0.25 there is no impact on the lower supporting structure. These observations are consistent with the constraint forces shown in chapter 2. There it was observed that as  $\lambda$  increases the region over which the net moment on the connecting rod which leads to impacts on the lower structure becomes smaller and moves towards the piston position corresponding to  $\theta = 0$ . For  $\lambda$  beyond a critical value, depending on  $\rho$ , over no range of crank angle intervals does the net moment push the connecting rod toward the lower structure. In such a case impacts will not generally occur on the lower structure during steady state operation.

To this point we have not varied the coefficient of restitution  $e$ . Reduction in the value of  $e$  has a predictable outcome: motions increase their sliding duration and



become periodic. This is true over all ranges of  $\lambda$  and  $\rho$  considered in this work. As an example we take  $(\lambda, \rho) = (0.05, 0.02)$  (a case considered with  $e = 0.9$  in section 4.3) and reduce  $e$ . This case is one in which the bearing dissipation is small (or the crank speed is high) and the gap is quite large, conditions ripe for chaos. Figures 4.21, 4.38, and 4.39 present the Poincare maps for  $e$  values of 0.9, 0.7, and 0.5. It can be seen that as the coefficient of restitution decreases, the response changes from chaotic to transient chaos and eventually periodic motion appears. Note that at values of  $e$  near unity no sliding occurs and as  $e$  decreases sliding occurs more often. Figures 4.8, 4.40, and 4.41 provide the impact distribution pattern for those values of the coefficient of restitution.

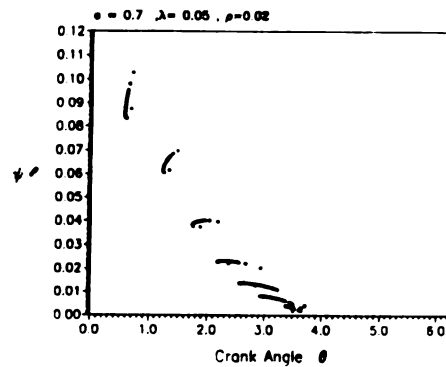


Figure 4.38: Poincare Map,  $e = 0.7$ ,  $\lambda = 0.05$ , and  $\rho = 0.02$

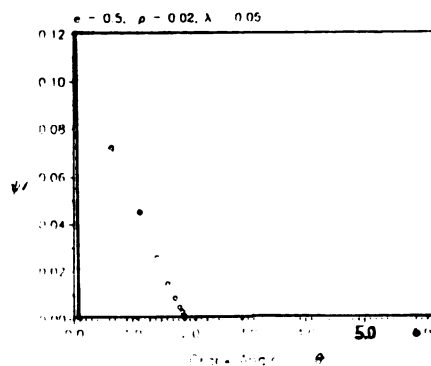


Figure 4.39: Poincare Map,  $e = 0.5$ ,  $\lambda = 0.05$ , and  $\rho = 0.02$

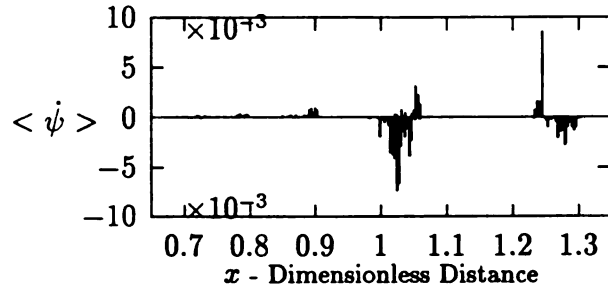


Figure 4.40: Impact Dist. Pattern,  $e = 0.7$ ,  $\lambda = 0.025$ , and  $\rho = 0.020$

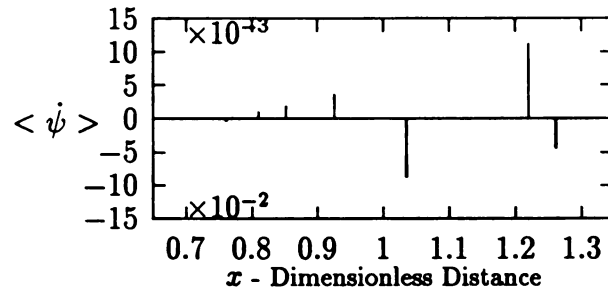


Figure 4.41: Impact Dist. Pattern,  $e = 0.5$ ,  $\lambda = 0.025$ , and  $\rho = 0.020$

Figures 4.42, 4.43, and 4.44 show results in the form of time traces over three crank revolutions for these three cases. As expected, the motion develops substantial sliding and becomes periodic. Note that in the limit  $e \rightarrow 0$  sliding will nearly always occur since the rebound velocity is zero. While transient chaos may occur even in the case of  $e = 0$ , periodic motions will dominate the response (see Shaw/Holmes [5]).

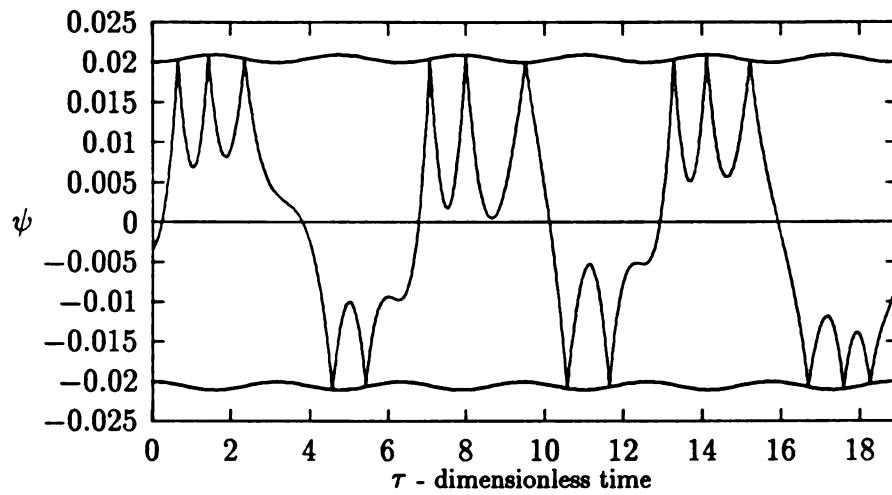


Figure 4.42: Time Trace,  $e = 0.9$ ,  $\lambda = 0.05$ , and  $\rho = 0.02$

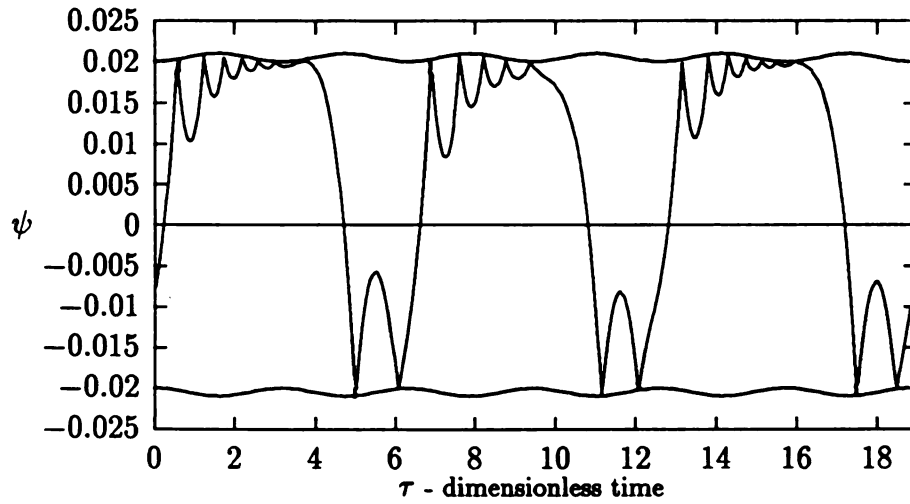


Figure 4.43: Time Trace,  $e = 0.7$ ,  $\lambda = 0.05$ , and  $\rho = 0.02$

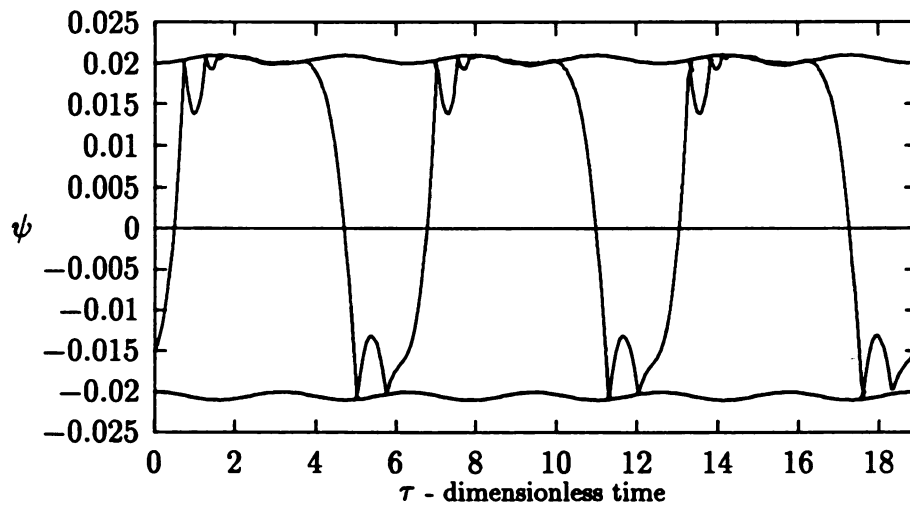


Figure 4.44: Time Trace,  $e = 0.5$ ,  $\lambda = 0.05$ , and  $\rho = 0.02$

## Chapter 5

# Discussions and Future Direction for Research

This study is a first step in a series of studies which should be carried out in order to more completely understand the dynamics of piston-slap. The model developed and investigated herein was designed so as to facilitate the analysis and simulations in order that some general observations could be made regarding the influence of various system parameters on the response of a slider-crank mechanism with slider clearance. Of particular interest was the possibility and characterization of chaotic motions in this system.

It has been shown that chaotic motions are prevalent over a range of parameters which correspond to high crank speeds and/or low bearing friction with relatively ideal impacts (that is, coefficient of restitution near to unity). In applications, one tends to design so as to minimize bearing friction in order to maximize efficiency and reduce energy consumption. This may have an additional benefit if it encourages

chaos (for the reasons given below). However, in typical automotive applications, the effective coefficient of restitution is on the order of  $e = 0.4$  (Fawcett and Wilson [11]) which indicates that sliding motions will most likely dominate the response of pistons in automotive engines. The data also indicates that impact velocities are more severe for larger gap sizes. This is expected and is due to the fact that the connecting rod/piston assembly has a longer time duration over which to build up momentum between impacts.

One must be very cautious in using information obtained from simulations of the type presented here due to their demonstrated sensitivity on parameter changes in the model and due to the limitations of the model itself. Due to this, it may be practically impossible to construct a model which is capable of predicting the nature of the system response over a range of speeds with any confidence. Chaos, transient chaos, and periodic motions are all possible and, in fact, due to the very possibility of transient chaos, it is possible to observe either chaos or periodicity for a given set of parameters depending entirely on the initial conditions and on the time scale over which the response is observed.

The results presented here indicate that chaotic motion may have a beneficial effect with regards to wear in mechanisms with clearances. This is simply due to the fact that the distribution of impacts is more uniform when the system responds in a chaotic manner than when the motion is periodic. The repeated impact patterns associated with periodic motions can lead to more highly localized wear. One must be careful in drawing too firm conclusions from this observation, however, since periodic motions with significant sliding may induce less wear than motions with a greater number of

impacts, independent of how well distributed they are. In addition, consideration of noise generation and fatigue may offset any potential benefits in reducing wear, since increases in sliding duration are typically correlated with fewer impacts per cycle. These are topics which lie outside the scope of this thesis, but should be considered in future work on this subject.

The statistical means of data presentation used in this thesis are, for two reasons, of more practical use than the Poincare maps which are typically used to present chaotic dynamics. First, by showing normalized average impact velocities after the completion of a long-term simulation, in place of individual velocities at each impact, one obtains an integral average measure which cannot be obtained from the pattern of the Poincare maps. Second, and more significant, is the fact that the impact distribution diagrams and impact spectra can be used for more complex models, including those with more than one degree of freedom, by indicating actual impact locations and impact velocities regardless of the particular configuration of the system at impact. In contrast, the Poincare map for even a two degree of freedom model (such as the one described below) contains *all* information about the state of the system at impact; it is four dimensional, and therefore difficult to represent in graphical form.

The following are some possible directions for improving the model for future studies:

- Consideration of the piston geometry. A first step in this direction would be to make the piston rectangular and include its dynamics, resulting in a two degree of freedom model.





- Consideration of an end-load acting on the piston. This would represent gas-pressure effects in engine applications.
- Non-symmetric placement of the connecting rod-piston bearing joint. This technique is currently used to suppress piston-slap ( [23]).
- Inclusion of friction in all bearing joints which influence the dynamics.

By implementing the above improvements, the resulting two degree of freedom model will provide a more accurate prediction of the motion of a piston in a cylinder.

## **Appendix A**

# Appendix A

## Derivation of $\psi_{max}$ and $\psi_{min}$

The maximum and minimum values of  $\psi$  that are possible due to the existence of the clearance are found by directly using the geometry of the model. Figure A.1

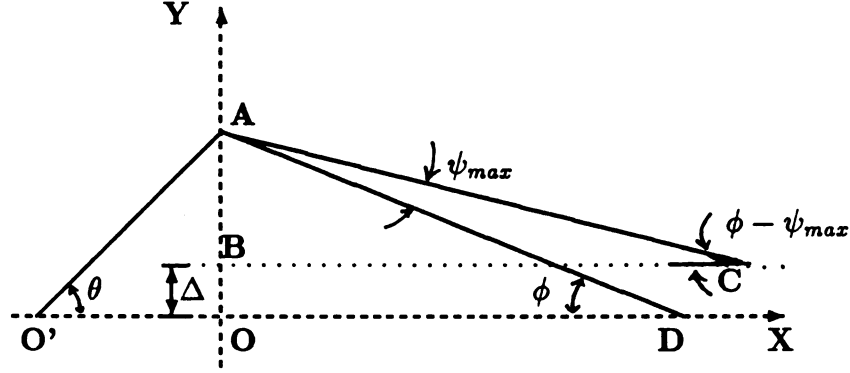


Figure A.1: The maximum angle

contains a schematic view of the model showing the connecting rod in its maximum possible position (i.e.  $\psi = \psi_{max}$ ). In this figure,  $O'$  corresponds to the center of crank rotation, line  $\overline{BC}$  corresponds to the line along which the slider center will travel when the roller moves along the upper slider boundary, and the  $X$ -axis corresponds to the

nominal path of center of the roller. Also,  $\Delta$  is the clearance that exists between the upper supporting structure and the upper edge of the roller (the size of  $\Delta$  is exaggerated in the Figure A.1 for clarity). Note that  $\psi_{max}$  depends on the crank angle  $\theta$ , or equivalently, is time dependent. Note also that as the gap size  $\Delta$  decreases to zero, the model approaches a system without clearance. The maximum possible angle is found by applying some simple trigonometric identities. Note that in this figure  $\overline{AD}$  is equal to  $\overline{AC}$  which is the length of the connecting rod (i.e.  $\overline{AD} = \overline{AC} = l$ ). Considering  $\triangle AOD$  we obtain

$$\overline{AO} = l \sin \phi$$

The height of  $\triangle ABC$  is

$$\overline{AB} = l \sin \phi - \Delta$$

and also the  $\angle ACB$  is known to be

$$\angle ACB = \phi - \psi_{max}$$

Using the following identity

$$\sin(\phi - \psi_{max}) = \frac{\overline{AB}}{\overline{AC}}$$

with the known values yields

$$\sin(\phi - \psi_{max}) = \frac{l \sin \phi - \Delta}{l} \quad (\text{A.1})$$

The rules of summation of angles results in

$$\sin \phi \cos \psi_{max} - \cos \phi \sin \psi_{max} = \frac{l \sin \phi - \Delta}{l}$$

For small gap sizes, and thus small angles  $\psi$ , a Taylor expansion in terms of  $\psi$  is employed. Using

$$\cos \psi = 1 + \mathcal{O}(\psi^2)$$

$$\sin \psi = \psi + \mathcal{O}(\psi^3)$$

and considering only linear terms in  $\psi$ , the following is obtained:

$$\sin \phi - \cos \phi \psi_{max} = \frac{l \sin \phi - \Delta}{l}$$

Solving for  $\psi_{max}$  gives

$$\psi_{max} = \frac{\Delta}{l \cos \phi} \quad (\text{A.2})$$

and recalling that

$$l \cos \phi = \sqrt{l^2 - r^2 \sin^2 \Omega t}$$

results in

$$\psi_{max} = \frac{\Delta}{\sqrt{l^2 - r^2 \sin^2 \Omega t}} \quad (A.3)$$

The dimensionless form is obtained by dividing through by  $l$  resulting in

$$\psi_{max} = \frac{\rho}{\sqrt{1 - \xi^2 \sin^2 \tau}} \quad (A.4)$$

where  $\rho$  is the dimensionless gap size given by

$$\rho = \frac{\Delta}{l}$$

where  $\Delta = d - r^*$  in the notation of section 2.5.

By applying a similar approach the minimum possible angle for the connecting rod can be found. It is given by

$$\psi_{min} = \frac{-\rho}{\sqrt{1 - \xi^2 \sin^2 \tau}} \quad (A.5)$$

Note that  $\psi_{max}$  and  $\psi_{min}$ , the maximum and minimum angles that the connecting rod can deviate from its nominal position due to the existence of the clearance, depend on the crank angle orientation as well as the system's fixed geometrical properties.

## **Appendix B**

# Appendix B

## Simulation Routine

The routine used for the simulations takes into consideration non-sliding motion and sliding motion. As a result, it is capable of handling a wide range of parameter values.

In this routine, the equation of motion (equation 2.13) is written in terms of two first order differential equations as given in section 3.1 (equations 3.2, 3.3). The two differential equations which describe the motion of the connecting rod angle are numerically solved by using a forth order Runge-Kutta method with a nominal step size of 0.005. Starting from some initial conditions inside the constraints and stepping through time, eventually a violation of the constraints on the roller occurs (i.e.  $x_1 > \psi_{max}$  or  $x_1 < \psi_{min}$ ). By using Newton's root solving method, the crank angle at which  $x_1 = \psi_{max}$  ( or  $x_1 = \psi_{min}$ ) is found. Then, the impact rule is applied and the post impact velocity is determined by equation 2.17. Once the post impact velocity and the location of the impact have been determined, the solver continues to solve for  $x_1$  and  $x_2$ , using these as initial locations for the free flight equations of motion. A period of 30 crank cycles is allowed for the system to achieve "steady



state“ and then the required data is collected over a a number of crank cycles (typically 1500 - 3000). Occasionally Newton’s method does not converge, for example when the impact velocity is very small. This difficulty occurs most frequently for larger values of  $\lambda$  , in which case the following procedure takes place. In such cases a reduced step size of 0.0001 is used for the integrator from the pre-impact point until the clearance condition is violated. If Newton’s method fails again, the step size is reduced further.

Whenever the relative post-impact velocity is less than some very small value,  $|\dot{\psi} - \dot{\psi}_{max}|$  or  $|\dot{\psi} - \dot{\psi}_{min}| < \epsilon$  ( $\epsilon = 0.005$  is used) , the roller is assumed to slide from that point until it is released at the crank angle at which the constraint force becomes zero. At this location the system will once again begin free flight with initial conditions of  $x_1 = \psi_{max}$  and  $x_2 = \dot{\psi}_{max}$  for the upper supporting structure and  $x_1 = \psi_{min}$  and  $x_2 = \dot{\psi}_{min}$  for the lower supporting structure. Figure B.1 provides a flow chart for the simulation routine for the dynamics of the system under investigation.

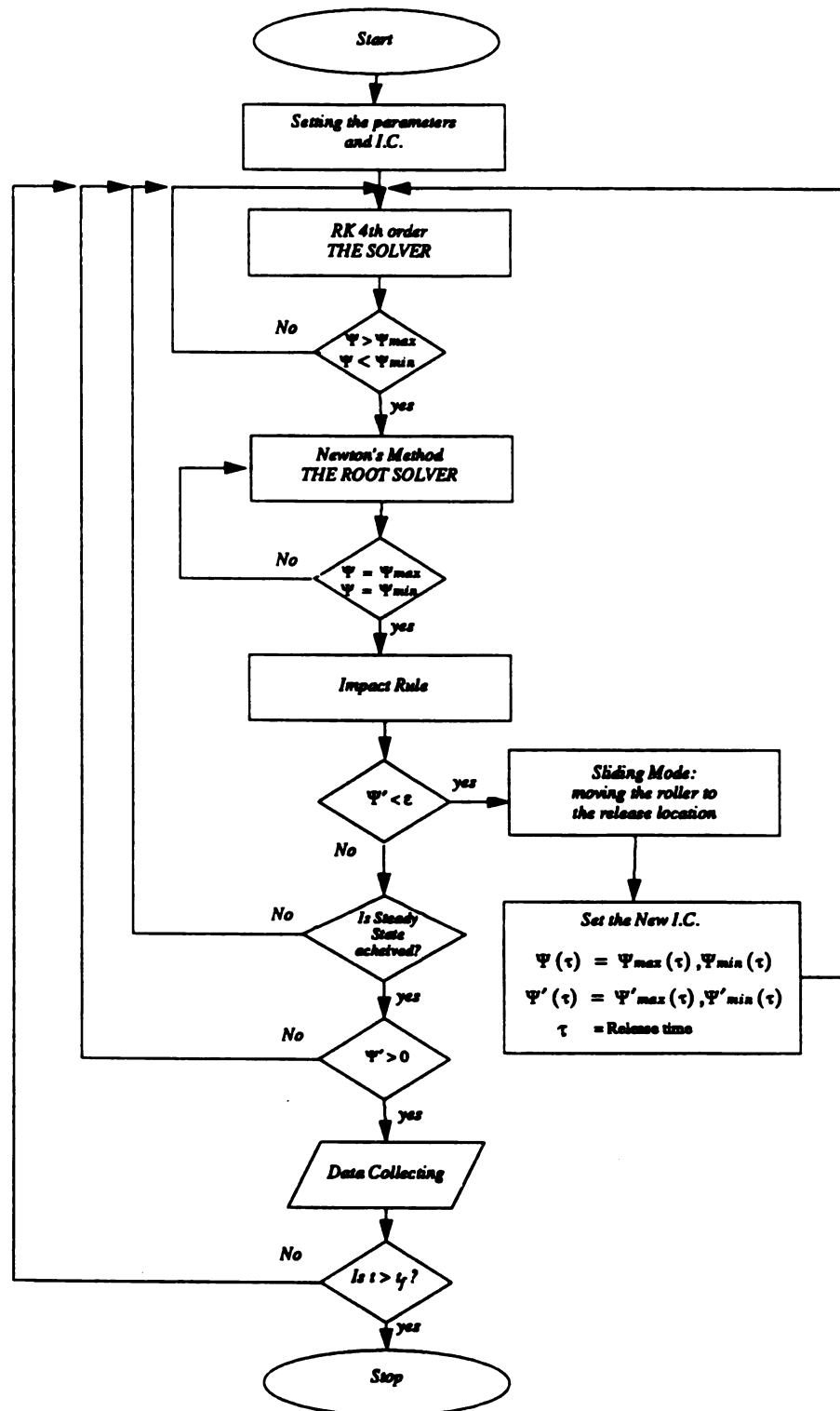


Figure B.1: Flow Chart: Simulation Routine

## **Bibliography**

# Bibliography

- [1] Shaw, Steven W., "The Dynamics of a Harmonically Excited System Having Rigid Amplitude Constraints Part 1: Sub-harmonic Motions and Global Bifurcations," *Journal of Applied Mechanics* ,Vol. 52, pp. 453-458, 1985.
- [2] Shaw, Steven W., "The Dynamics of a Harmonically Excited System Having Rigid Amplitude Constraints Part 2: Chaotic Motions and Global Bifurcation," *Journal of Applied Mechanics* ,Vol. 52, pp. 459-464, 1985.
- [3] Shaw, Steven W., "Forced Vibration of a Beam with One-Sided Amplitude Constraint: Theory and Experiment," *Journal of Sound and Vibration* ,Vol 99, pp. 199-212, 1983.
- [4] Shaw, Steven W., and Holmes, P. J., "A Periodically Forced Piecewise Linear Oscillator," *Journal of Sound and Vibration* ,Vol 90, pp. 129-155, 1983.
- [5] Shaw, Steven W., and Holmes, P. J., "A Periodically Forced Impact Oscillator with Large Dissipation," *Journal of Applied Mechanics*, Vol. 105, pp. 849-857, 1983.
- [6] Miedema,B. ,and Mansour, W. M., "Mechanical Joints With Clearance: a Three-Mode Modal," *Journal of Engineering for Industry*, pp.1319-1323, 1976.
- [7] Granat, S. J. , and Fawcett, "Effects of clearance at the Coupler-Rocker Bearing of a 4-Bar Linkage," *Mechanism and Machine Theory*, Vol. 14, pp. 99-110, 1979.
- [8] Dubowsky, S. , Norris, M., Aloni, E. ,and Tamir A. , "An Analytical and Experimental Study of the Prediction of Impacts in Planar Mechanical Systems With Clearances," *Journal of Mechanisms Transmissions and Automation Design*, pp. 1-8, 1984.
- [9] Mansour, W. M., and Townsend, M.A., "Impact Spectra and Intensities for High-Speed Mechanisms," *Journal of Engineering for Industry*, pp. 347-358, 1975.
- [10] Dubowsky, S. , "On Predicting the Dynamic Effects of Clearances in Planar Mechanisms," *Journal of Engineering for Industry*, pp. 317-323, 1974.
- [11] Wilson, R. , and Fawcett,J. N., "Dynamics of the Slider-Crank Mechanism with Clearance in the Sliding Bearing," *Mechanism and Machine Theory*, Vol. 9, pp. 61-80, 1974.

- [12] Denman, H. H. , "Exact Solution for the Free Rigid Slider-Crank Mechanism," *Mechanism and Machine Theory*, Vol. 23, No. 6, pp. 435-439, 1988.
- [13] Karagiannis, K., "Simulation sergebnisse eines einstugigen Getriebes," *Fortschritt-Berichte VDI*, Reihe 11 Schwing ung stechnik, Nr. 125, 1989.
- [14] Pfeiffer, F., and Kunert, A. , "Rattling Models from Deterministic to Stochastic process," *Nonlinear Dynamics*, Vol. 1, No.1 , pp. 63-74, 1990.
- [15] Haines, R.S., "A Theory of Contact Loss at Revolute Joints With Clearance," *Journal of Mechanical Engineering Science*, Vol. 22 No. 3, pp. 129-136, 1980.
- [16] Wu, C. L. S., and Earles, S.W.E., "A Determination of Contact-Loss at a Bearing of a Linkage Mechanism," *ASME Journal of Engineering for Industry*, paper No. 76-DET-43, pp. 375-380, 1977.
- [17] Townsend, M. A., and Mansour, W. M., "A Pendulating Model for Mechanisms With Clearance in the Revolutes," *ASME Journal of Engineering for Industry*, paper No. 74-DET-22, pp.354-358, 1975.
- [18] Dubowsky, S., and Gardener, T. N., "Design Analysis of Multi-link Felixible Mechanisms with Multiple Clearance Connections," *ASME Journal of Engineering for Industry*, 1976.
- [19] Dubowsky, S., and Gardener, T. N., "Dynamic Interactions of Link Elasticity and Clearance Connections in Planar Mechanical Systems," *ASME Journal of Engineering for Industry*, pp. 652-661, 1975.
- [20] Osman,M. O., Bahgat, B. M., and Sankar, T. S., "On the Dynamic Analysis of Planar Mechanisms with Multiple Clearance," *Journal of Mechanical Engineering Science*, Vol. 197C, pp. 89-95, 1983.
- [21] Garret, R. E., and Hall, A. S. , "Effects of Tolerance and Clearance in Linkage Design," *ASME Journal of Engineering for Industry*, pp. 198-202, 1969.
- [22] Whiston, G. S., "The Vibro-Impact Response of a Harmonically Exited and Pre-loaded One-Dimensional Linear Oscillator," *Journal of Sound and Vibration*, Vol. 115, pp. 303-319, 1987.
- [23] Burrell, G., and Butler, G., "A Study in Applied Physics: Locating the Piston Pin to Minimize Piston Slap," *General Motors Engineering Journal*, pp 38-43, Nov.-Dec. 1953.
- [24] Brach, R. M., *Mechanical Impact Dynamics, Rigid Body Collisions*, John Wiley and Sons, 1991.
- [25] Greenwood, D. T., *Principles of Dynamics, Second Edition*, Prentice Hall, pp. 160-161, 1988.
- [26] Moon, F. C., *Chaotic Vibrations*, Wiley, New York, 1987.

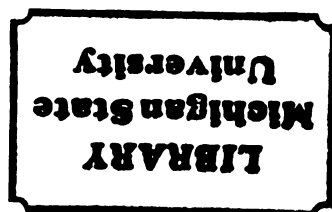
PLACE IN RETURN BOX to remove this checkout from your record.  
TO AVOID FINES return on or before date due.

DATE DUE    DATE DUE    DATE DUE

_____	_____	_____
_____	_____	_____
_____	_____	_____
_____	_____	_____
_____	_____	_____
_____	_____	_____
_____	_____	_____

MSU is An Affirmative Action/Equal Opportunity Institution

c:\circ\dms\dms.pn3-p.1



MICHIGAN STATE UNIV. LIBRARIES



31293009096417